Jupiter's auroral-related stratospheric heating and chemistry II: analysis of IRTF-TEXES spectra measured in December 2014

J. A. Sinclair[a,*], G. S. Orton[a], T. K. Greathouse[b], L. N. Fletcher[c], J. I. Moses[d], V. Hue[b], P. G. J. Irwin[e]

[a] *Jet Propulsion Laboratory/ California Institute of Technology, 4800 Oak Grove Dr, Pasadena, CA 91109, United States*
[b] *Southwest Research Institute, 6220 Culebra Rd., San Antonio, TX 78236, United States*
[c] *Department of Physics & Astronomy, University of Leicester, University Road, Leicester, LE1 7RH, United Kingdom*
[d] *Space Science Institute, 4750 Walnut St, Suite 205, Boulder, CO 80301, United States*
[e] *Atmospheric, Oceanic & Planetary Physics, University of Oxford, Parks Road, Oxford, OX1 3PU, United Kingdom*

Abstract

We present a retrieval analysis of TEXES (Texas Echelon Cross Echelle Spectrograph (Lacy et al., 2002)) spectra of Jupiter's high latitudes obtained on NASA's Infrared Telescope Facility on December 10-11th 2014. The vertical temperature profile and vertical profiles of C_2H_2, C_2H_4 and C_2H_6 were retrieved at both high-northern and high-southern latitudes and results were compared in 'quiescent' regions and regions known to be affected by Jupiter's aurora in order to highlight how auroral processes modify the thermal structure and hydrocarbon chemistry of the stratosphere. In qualitative agreement with Sinclair et al. (2017a), we find temperatures in auroral regions to be elevated with respect to quiescent regions at two discrete pressures levels at approximately 1 mbar and 0.01 mbar. For example, in comparing retrieved temperatures at 70°N, 60°W (a representative quiescent region) and 70°N, 180°W (centred on the northern auroral oval), temperatures increase by 19.0 ± 4.2 K at 0.98 mbar, 20.8 ± 3.9 K at 0.01 mbar but only by 8.3 ± 4.9 K at the intermediate level of 0.1 mbar. We conclude that elevated temperatures at 0.01 mbar result from heating by joule resistance of the atmosphere and the energy imparted by electron and ion precipitation. However, temperatures at 1 mbar are considered to result either from heating by shortwave radiation of aurorally-produced haze particulates or precipitation of higher energy population of charged particles. Our former conclusion would be consistent with results of auroral-chemistry models, that predict the highest number densities of aurorally-produced haze particles at this pressure level (Wong et al., 2000, 2003). C_2H_2 and C_2H_4 exhibit enrichments but C_2H_6 remains constant within uncertainty when comparing retrieved concentrations in the northern auroral region with quiescent longitudes in the same latitude band. At 1 mbar, C_2H_2 increases from 278.4 ± 40.3 ppbv at 70°N, 60°W to 564.4 ± 72.0 ppbv at 70°N, 180°W and at 0.01 mbar, over the same longitude range at 70°N, C_2H_4 increases from 0.669 ± 0.129 ppmv to 6.509 ± 0.811 ppmv. However, we note that non-LTE (local thermodynamic equilibrium) emission may affect the cores of the strongest C_2H_2 and C_2H_4 lines on the northern auroral region, which may be a possible source of error in our derived concentrations. We retrieved concentrations of C_2H_6 at 1 mbar of 9.03 ± 0.98 ppmv at 70°N, 60°W and 7.66 ± 0.70 ppmv at 70°N, 180°W. Thus, C_2H_6's concentration appears constant (within uncertainty) as a function of longitude at 70°N.

Keywords:

1. Introduction

Auroral processes on Jupiter are evident over a large range in wavelengths. X-ray, ultraviolet (UV), visible and near-infrared H_3^+ emission results from the precipitation of charged particles into the upper ionosphere of Jupiter where field lines intersect the atmosphere (e.g. Nichols et al. 2007; Ozak et al. 2010; Stallard et al. 2012). Jupiter's auroral regions also exhibit enhanced mid-infrared emission from CH_4 (7.8 μm), C_2H_2 (13 μm), C_2H_4 (10.5 μm), C_2H_6 (12.2 μm), which indicates that auroral processes also perturb the thermal structure and composition of the stratosphere at pressures between 10 mbar and 10 μbar (Caldwell et al., 1980; Kim et al., 1985; Drossart et al., 1993; Kostiuk et al., 1993; Livengood et al., 1993).

The magnitude of mid-infrared emission of C_2H_2, C_2H_4, C_2H_6 and further hydrocarbons depends both on the temperature of the line-forming region as well as the abundance of the emitting species. This degeneracy in temperature and composition has hindered several previous studies in quantifying whether the enhanced mid-infrared auroral emission of C_2H_2, C_2H_4 and further hydrocarbons results solely from enhanced temperatures or modified concentrations of the emitting species. However, in part I of this paper (Sinclair et al., 2017a), henceforth described as Paper I, we performed a retrieval analysis of Voyager 1-IRIS (Infrared Interferometer Spectrometer and Radiometer, Hanel et al. 1980) spectra acquired in 1979 and Cassini-CIRS (Composite Infrared Spectrometer, Flasar et al. 2004) spectra acquired in 2001 in order to reduce this degeneracy. Under the assumption that the vertical profile of CH_4 does not vary spatially (Moses et al., 2005), CH_4 emission (1230 - 1380 cm^{-1}) was used to retrieve the vertical temperature profile while the emission features of C_2H_2 and C_2H_6 were retrieved from their emission features (710 - 750 cm^{-1} and 770 - 890 cm^{-1} respectively). The temperature retrieval results of Cassini-CIRS $\Delta\tilde{\nu}$=0.5 cm^{-1} and 2.5 cm^{-1} observations indicated that temperatures in auroral regions were elevated in two discrete pressure ranges - 10 μbar and lower and the 1-mbar level - with respect to temperatures at quiescent longitudes.

*Corresponding Author
Email address: james.sinclair@jpl.nasa.gov (J. A. Sinclair)

This demonstrates that auroral processes heat the atmosphere in these two pressure ranges and we found this to be true in both the northern and southern auroral regions. High temperatures at pressures of 10 μbar and lower were concluded to be a result of heating by ion/electron precipitation and joule-heating in the atmosphere. However, we concluded that high temperatures at the 1 mbar were a result of either aurorally-produced haze particles heated by shortwave radiation or precipitation of a higher-energy population of charged particles. Retrievals of C_2H_2 and C_2H_6 indicated that the former was enriched while the latter was depleted in auroral regions with respect to quiescent regions. By analogy with ion-neutral chemistry models of Titan (De La Haye et al., 2008), we inferred that the dominance of ion-neutral chemistry within the auroral regions increases the production rates of all C_2 hydrocarbons, but in particular the unsaturated C_2H_2 and C_2H_4. Auroral activity continually enriches these hydrocarbons, but especially C_2H_2 and C_2H_4, while polar winds advect these hydrocarbons out of the auroral region. Once outside the auroral region, neutral photochemistry dominates over ion-neutral chemistry and readily converts C_2H_2 and C_2H_4 into C_2H_6. Thus, C_2H_6 is enriched outside the aurora and therefore appears depleted inside the auroral region. We direct the reader to Sinclair et al. (2017a) for further details and discussion of these results.

In this study, we seek to perform a similar analysis of IRTF-TEXES (Texas Echelon Cross Echelle Spectograph on NASA's Infrared Telescope Facility, Lacy et al. 2002) observations obtained in December 2014. The use of TEXES spectra presents many advantages over using the infrared datasets from Voyager and Cassini. Firstly, TEXES can operate at superior spectral resolutions (R ≤ 85000). At these high spectral resolutions, which exceed the highest-resolution Cassini-CIRS settings by a factor of 24, the weak and strong emission line features of CH_4 and other hydrocarbons are resolved in the spectrum of Jupiter, which allows a larger vertical range in the atmosphere to be sounded. This is particularly beneficial in the study of auroral processes on Jupiter since auroral-related heating and chemistry is expected generally to affect lower pressures to a greater magnitude. In addition, the higher vertical resolutions provided by the high spectral resolution allows for improved discrimination of upper and lower stratospheric effects. The second advantage of TEXES is the opportunity for future, follow-up observations, which will allow the evolution of auroral heating/chemistry of the stratosphere to be studied. While Voyager-IRIS in 1979, Cassini-CIRS in 2001 and IRTF-TEXES in 2014 observations do capture Jupiter's auroral stratosphere at many different epochs, making inferences of the evolution of Jupiter's aurora between these datasets was generally a challenge because of large differences in the spectral resolution (and therefore vertical resolution in the atmosphere), the spatial sampling on the planet and the overall global evolution of the planet over these long timescales.

The structure of this paper is as follows. In Section 2, we detail the TEXES instrument and the observing modes used to obtain spatially-resolved spectra of Jupiter's high latitudes. Section 3 details the radiative transfer modelling of TEXES spectra and Sections 4 and 5 then detail the results of temperature, C_2H_2, C_2H_4 and C_2H_6 retrievals from observed TEXES spectra on December 10-11th, 2014. In Appendix A, we explored the radiometric calibration of the spectra by applying scale factors ranging from 0.4 to 2.2 to the observed radiances and determining whether the fit to the spectra (quantified using the reduced χ^2 statistic) improved.

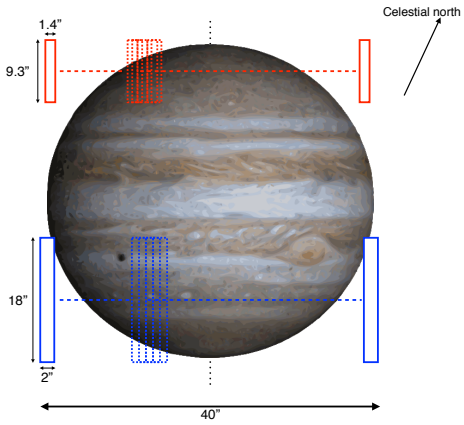

Figure 1: A schematic of the slit positions during scans of the north and south pole. The 9" x 1.4" (arcsec) slit is shown in red and the 18" x 2" slit is shown in blue and are shown to scale relative to the angular diameter of Jupiter of 40". It should be noted that both the 9" and 18" slits were used at each pole: for the sake of clarity, only one is shown at each pole.

2. Observations

The TEXES instrument (Texas Echelon Cross Echelle Specotrograph, Lacy et al. 2002) is a ground-based grating spectrometer that measures spatially-resolved spectra in the M (4.5- to 5.1-μm), N (7- to 13-μm) and Q bands (17- to 25-μm) at spectral resolving powers from R = 4000 to as high as 85000 (Lacy et al., 2002). In this work, we used high-resolution TEXES spectra with resolving powers from 60000 - 85000.

2.1. Data acquisition

We acquired spectra of Jupiter's high-southern and high-northern latitudes on December 11th 2014, when the sub-observer and sub-solar latitudes were 0.2°S and 0.28°N. Table 1 lists details of the five spectral settings used to measure the emission of H_2 S(1), C_2H_2, C_2H_6, C_2H_4 and CH_4. The slit was aligned parallel to Jupiter's rotational axis and initially positioned over dark sky west of the north polar region (see Figure 1). Initially, an exposure was performed of a room-temperature blackbody (a high-emissivity chopper blade) fixed in the fore-optics of the TEXES instrument, which

Setting Name	Wavenumber range (cm^{-1})	Target spectral feature	Resolving power ($\Delta\tilde{\nu}/\tilde{\nu}$)	Slit length (arcsec)	Slit width (arcsec)	Diffraction-limited spatial resolution (arcsec)
587	585.8 - 588.7	H_2 S(1)	60000	18.7	2	1.43
730	728.8 - 732.6	C_2H_2	85000	9.3	1.4	1.15
819	816.2 - 822.7	C_2H_6	85000	9.3	1.4	1.02
950	947.3- 953.3	C_2H_4	85000	9.3	1.4	0.88
1248	1244.5 - 1250.7	CH_4	85000	9.3	1.4	0.67

Table 1: The details of the spectral settings for which spectra were obtained of Jupiter's high latitudes.

served as both a radiometric calibrator and flat-field. In the 587 cm^{-1} setting, the slit was stepped east in approximately 40 increments of 1 arcsec each (using half the slit-width in order to obtain Nyquist spatial sampling) and a 2-second exposure was performed at each step. The scan was then repeated as a contingency in case one of the scans was poor in quality. The slit was then slewed to an equivalent position over dark sky west of the southern polar region and a similar scan was performed in order to obtain spectra of high-southern latitudes. Each north-south scan pair (representing a total of four scans, two for each pole) was then repeated for the remaining spectral settings. In these latter four settings, the slit step across the planet was set to 0.7 arcsec such that sampling remained at half a slit-width.

Each set of north-south polar scan pairs over all spectral settings formed a data *cube* of spectra of H_2 S(1), C_2H_2, C_2H_6, C_2H_4 and CH_4 emission as a function of latitude and longitude over both north and south polar regions and dark-sky regions east and west of each pole. Further data cubes were acquired while using the rotation of Jupiter (on a period of approximately 9.8 hours) to gain further longitudinal coverage.

2.2. Reduction & calibration

The TEXES data reduction package (Lacy et al., 2002) was used to reduce and calibration each data cube. The coverage of dark sky allowed subtraction of sky emission from the spectra covering the disk of Jupiter. In addition, the exposure of the room-temperature blackbody of known temperature was differenced by the sky-emission and allowed the absolute calibration of target spectra into units of radiance. The blackbody exposure was also normalised and adopted as a flatfield measurement to remove pixel-to-pixel sensitivity variations and other detector artefacts from the spectral-spatial images. A custom-designed IDL pipeline was used to map the spectra by longitude, latitude, emission angle and determine the combined radial velocity of each point on the planet (as a result of Jupiter's radial motion to/from the observer and the rotational motion of Jupiter). All spectra were doppler shifted into the rest frame. The details of the reduction, calibration and mapping are provided in greater detail in Fletcher et al. (2016), who used lower resolution TEXES spectra at lower latitudes.

The noise-equivalent spectral radiance (or NESR) associated with each target spectrum was calculated by computing the standard deviation in radiance at each wavenumber for all dark-sky pixels more than 2 arcseconds away from the limb of Jupiter. This calculation of the noise therefore accounted for the random noise associated with the sensitivity of the instrument and also the contamination of the spectrum in wavenumber ranges of poor telluric transmission. Such wavenumber ranges are higher in noise and therefore are weighted less in subsequent retrieval analyses.

2.3. Spatial coaddition

All individual spectra were averaged into latitude-longitude bins. Latitude bins were 4° in planetographic latitude, stepped in increments of 2° for Nyquist-sampling and longitude bins were 20° in size, stepped in increments of 10°. The largest of either: 1) the NESR spectrum multiplied by a factor of $1/\sqrt{N}$, where N is the number of individual spectra coadded or 2) the standard error on the coadded (mean) radiance was adopted as the effective uncertainty on the radiance.

Figure 2 shows polar projections of brightness temperature as a function of latitude and longitude for line emission of H_2 S(1), CH_4, C_2H_2, C_2H_4 and C_2H_6. Enhanced auroral-related emission is evident in the brightness temperatures of the hydrocarbon species, in particular C_2H_2 and C_2H_4, at high-northern latitudes centred on System III longitudes of 180°W. This is coincident with the ultraviolet oval features (Bonfond et al., 2012). The effects of the southern auroral region are less evident due to its position at a comparably higher latitude together with the sub-observer latitude favoring visibility of high-northern latitudes. Nevertheless, the edges of the long-axis of the southern auroral oval feature are visible, in particular in C_2H_2 and C_2H_4 emission, at approximately 60°W and 240°W. The inversion of the vertical temperature profile and the vertical profiles of C_2H_2, C_2H_4 and C_2H_6 will determine whether the enhanced emission of these species in auroral regions results from warmer temperatures and/or changed in the concentrations these species. Section 3 details the forward modelling and retrieval methods adopted in this work.

3. Radiative transfer modelling

The radiative transfer modeling approaches adopted in this work are very similar to those presented in Sinclair et al.

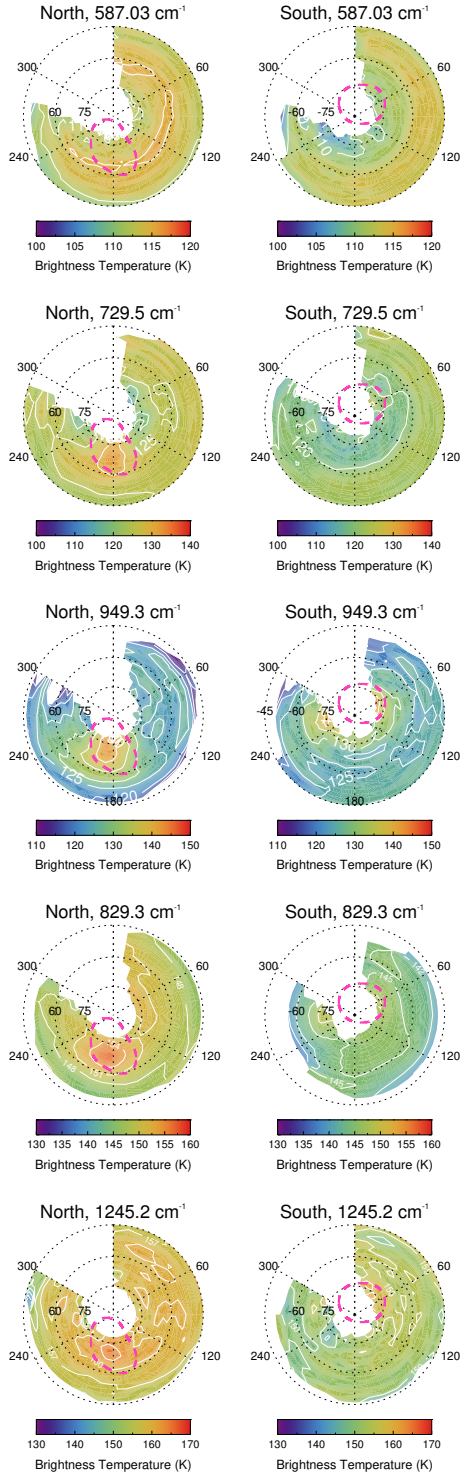

Figure 2: Northern (1st column) and southern (2nd column) polar projections of the brightness temperature at 587.03 cm^{-1} (1st row), 729.5 cm^{-1} (2nd row), 949.3 cm^{-1} (3rd row), 829.3 cm^{-1} (4th row) and 1245.2 cm^{-1} (bottom) corresponding to H_2 S(1), C_2H_2, C_2H_4, C_2H_6 and CH_4 emission respectively. The position of the auroral oval features in the ultraviolet (Bonfond et al., 2012) are shown as dashed, red lines.

(2017a). We have adopted the same *reference* model jovian atmosphere, which is based on a mean of temperatures from 30°S to 30°N retrieved in Fletcher et al. (2009) and Nixon et al. (2010). However, alternative temperature profiles are also tested in performing retrievals. The vertical profiles of CH_4 and its isotopologues are adopted from Romani (1996) and the vertical profiles of all remaining hydrocarbons were assumed from the photochemical model by Moses et al. (2005). Further details of the model atmosphere are provided in Section 3 of Sinclair et al. (2017a).

The forward modelling and retrieval of spectra in this work were conducted using NEMESIS (Irwin et al., 2008). While NEMESIS can perform modelling using both line-by-line and the correlated-k method, we have opted for the latter approach given its higher computational efficiency. Test spectra forward modelled using the correlated-k method and the line-by-line method were in agreement within 10%, which was generally smaller than the 1-σ noise on the measured spectra. Spectroscopic line parameters in this work are identical to those presented in Fletcher et al. (2016), which includes the line parameters for the H_2 S(1) line at 587.03 cm^{-1}. For H_2, CH_4, CH_3D, $^{13}CH_4$, C_2H_2, C_2H_4, C_2H_6, PH_3, NH_3, k-distributions using a 4 km s^{-1} sinc-squared convolution were computed from 728 to 733 cm^{-1}, 818 to 823 cm^{-1}, 947 to 953 cm^{-1} and 1244 to 1252 cm^{-1} in order to model TEXES spectra acquired in the corresponding spectral settings. This results in a spectral resolution ranging from 0.0097 cm^{-1} in the 730 cm^{-1} setting to 0.0166 cm^{-1} in the 1248 cm^{-1} setting. A 6 km s^{-1} sinc-squared convolution (or 0.011 cm^{-1} spectral resolution) was adopted in calculating the k-distributions in the 587 cm^{-1} setting due to the wider slit width.

4. Temperature results

The vertical temperature profile was retrieved simultaneously from the H_2 S(1) and CH_4 emission features in the 587 cm^{-1} and 1248 cm^{-1} settings. For reasons detailed in Appendix A, a factor of 1.25 has been applied to all radiances of spectra in the 587 cm^{-1} since this improved the fit to the H_2 S(1) emission feature while simultaneously fitting CH_4 emission features in the 1248 setting. The following spectral regions were selected in order to capture H_2 S(1) emission and a mixture of weak and strong lines of CH_4 emission, whilst avoiding unphysical regions of zero radiance in the spectra corresponding to wavenumbers missed by the grating: 587.0 - 587.1 cm^{-1}, 1245.18 - 1246.0 cm^{-1}, 1246.45 - 1246.90 cm^{-1}, 1247.82 - 1249.0 cm^{-1}, 1249.6 - 1250.3 cm^{-1}.

4.1. Vertical sensitivity

Figure 3 shows the vertical functional derivatives in these spectral regions with respect to temperature in the retrievals at 70°N, 60°W and 70°N, 180°W, which respectively exemplify quiescent and auroral longitudes. In quiescent conditions away from the auroral region, H_2 S(1) and CH_4 emission provide sensitivity over the 20- to 1-mbar and 10- to 0.01-mbar

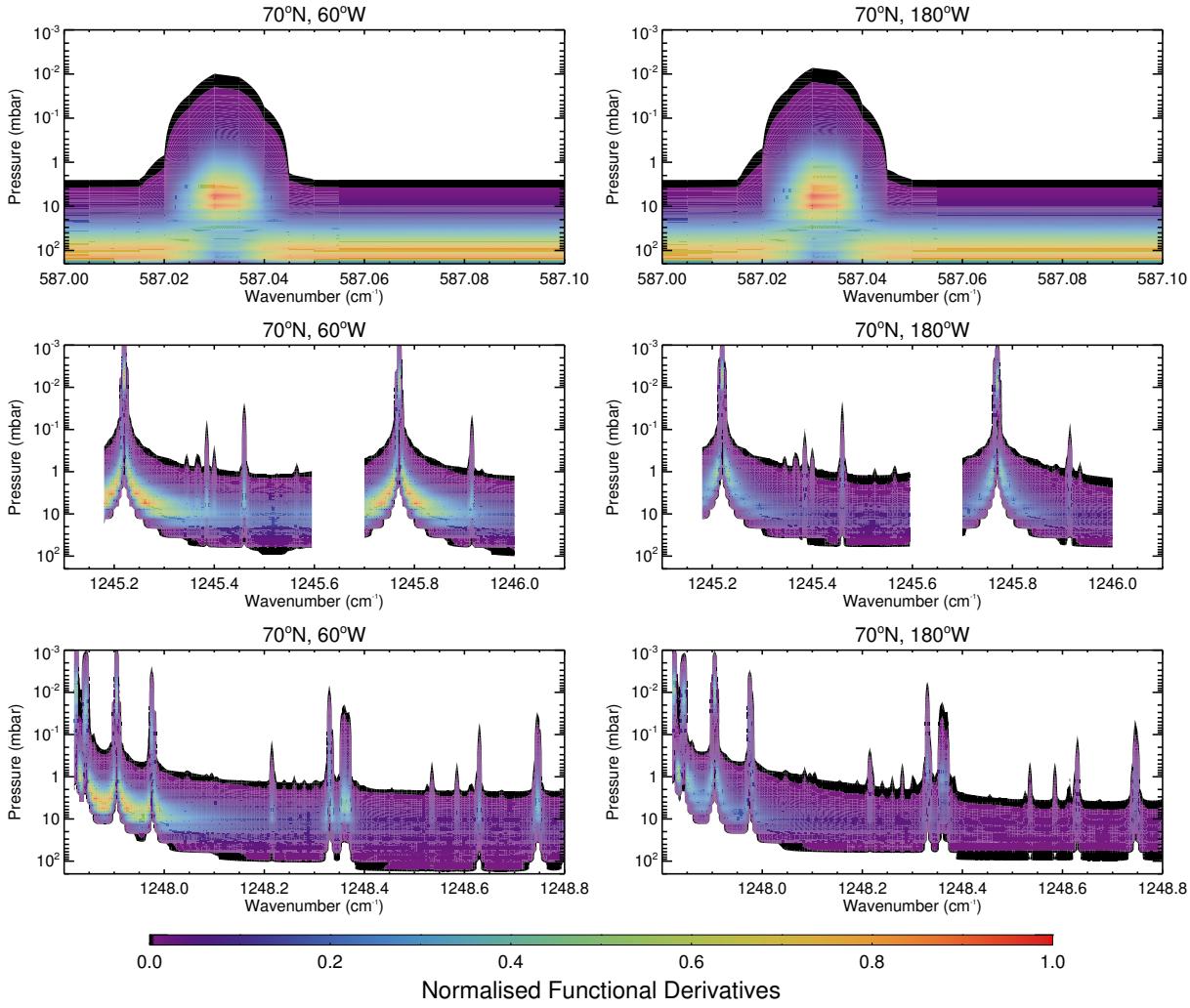

Figure 3: The absolute, normalised, vertical functional derivatives for temperature at 70°N, 60°W (left) and 70°N, 180°W (right) in the 587 cm^{-1} setting (top) and 1248 settings (2nd and 3rd row). For brevity, only a representative subset of the 1248 setting is shown.

pressure ranges respectively. In auroral conditions, there is negligible change in the vertical sensitivity provided by the H_2 S(1) setting. However, the sensitivity to temperature in the 1248 cm^{-1} setting in the upper stratosphere (at pressures lower than 0.1 mbar) increases in auroral conditions, which is intuitive given the presence of high temperatures at such altitudes. However, in both quiescent and auroral conditions, the 587 cm^{-1} and 1248 cm^{-1} settings together provide sensitivity from 10 mbar to 5 µbar. We will present retrieved temperatures at four representative pressure levels within this range of sensitivity: 4.7 mbar, 0.98 mbar, 0.1 mbar and 0.01 mbar.

4.2. Temperature distributions

Figure 4 shows the distributions of retrieved temperature at four pressure levels at both high-northern and high-southern latitudes. As shown, auroral-related heating is evident at longitudes coincident with auroral emission observed at ultraviolet wavelengths. In both the northern and southern auroral regions, there is no evidence of warm stratospheric temperatures at pressures higher than the 1-mbar level. In the 1-mbar to 10-µbar pressure range, over which there is evidence of auroral-related heating, the enhancement of temperature appears highest at the 10-µbar level and 1-mbar levels, with a comparably lesser enhancement at the 0.1-mbar level. For example, in comparing retrieved temperatures at 70°N, 60°W (a northern quiescent region) and 70°N, 180°W (the northern auroral hotspot), the temperature increases by 19.0 ± 4.2 K, 8.3 ± 4.9 K and 20.8 ± 3.9 K at 1 mbar, 0.1 mbar and 0.01 mbar respectively. This behaviour is qualitiatively consistent with the analysis of Cassini-CIRS spectra in Sinclair et al. (2017a).

The bifurcation of the temperature profile in auroral regions is further demonstrated in Figure 5, which compares model-data spectra and the corresponding retrieved temperature profiles in quiescent and auroral locations in the north and south. As shown, retrieved temperature profiles in the auroral regions at 70°N, 180°W and 74°S, 60°W both exhibit a maximum at

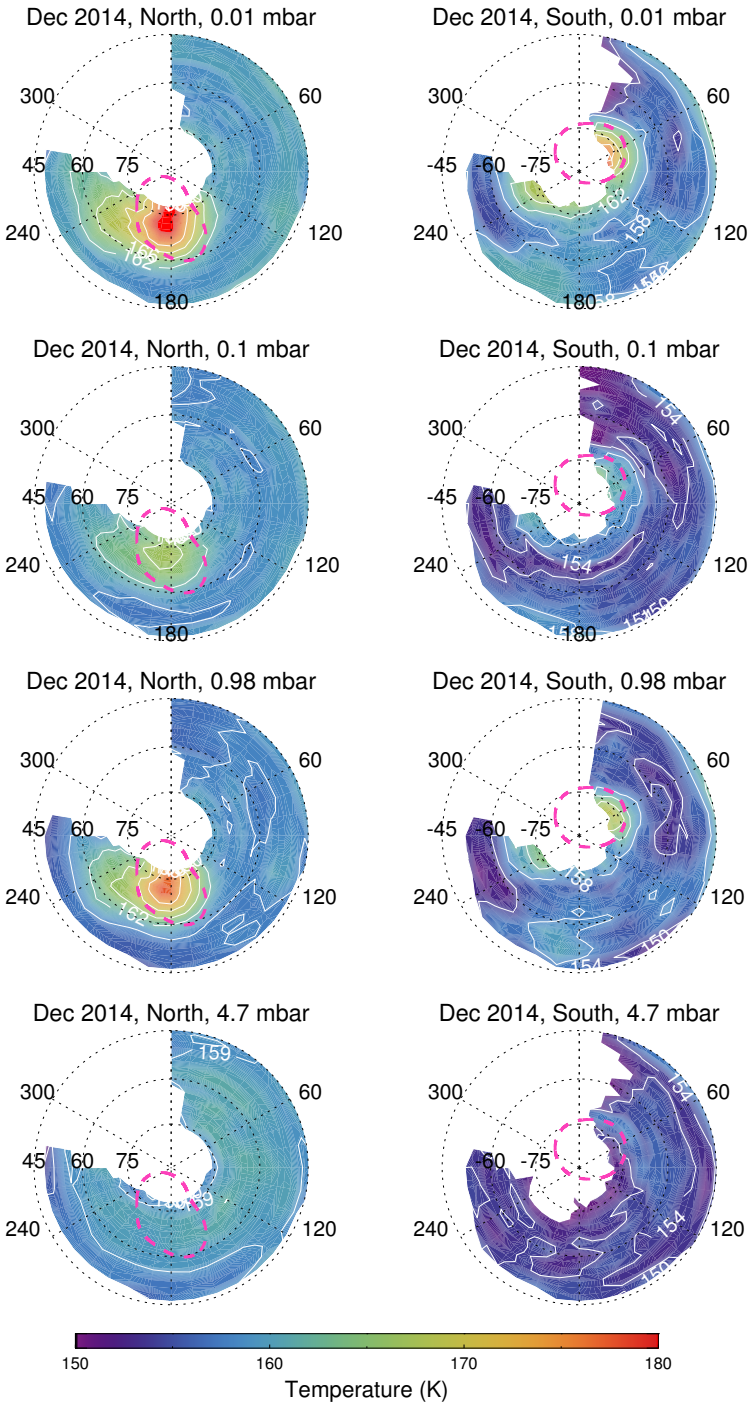

Figure 4: Polar projections of retrieved temperature distributions at 4.7 mbar (top), 0.98 mbar (2nd row), 0.1 mbar (3rd row) and 0.01 mbar (4th row) in the north (left column) and south (right column). Dashed, red lines show the positions of the ultraviolet auroral ovals as measured by Bonfond et al. (2012).

approximately the 1-mbar level and a minimum in temperature at the 0.1-mbar level. Such features are absent from the retrieved temperature profiles at quiescent longitudes in the same latitude band. From 0.1 mbar to 10 µbar, temperatures in the auroral region rise and then tend back to the *a priori* profile at pressures lower than 5 µbar where there is no sensitivity in the observations (Figure 3).

4.3. Testing alternative a priori

In order to test the robustness of retrieved vertical profiles of temperature, we performed further retrievals starting from

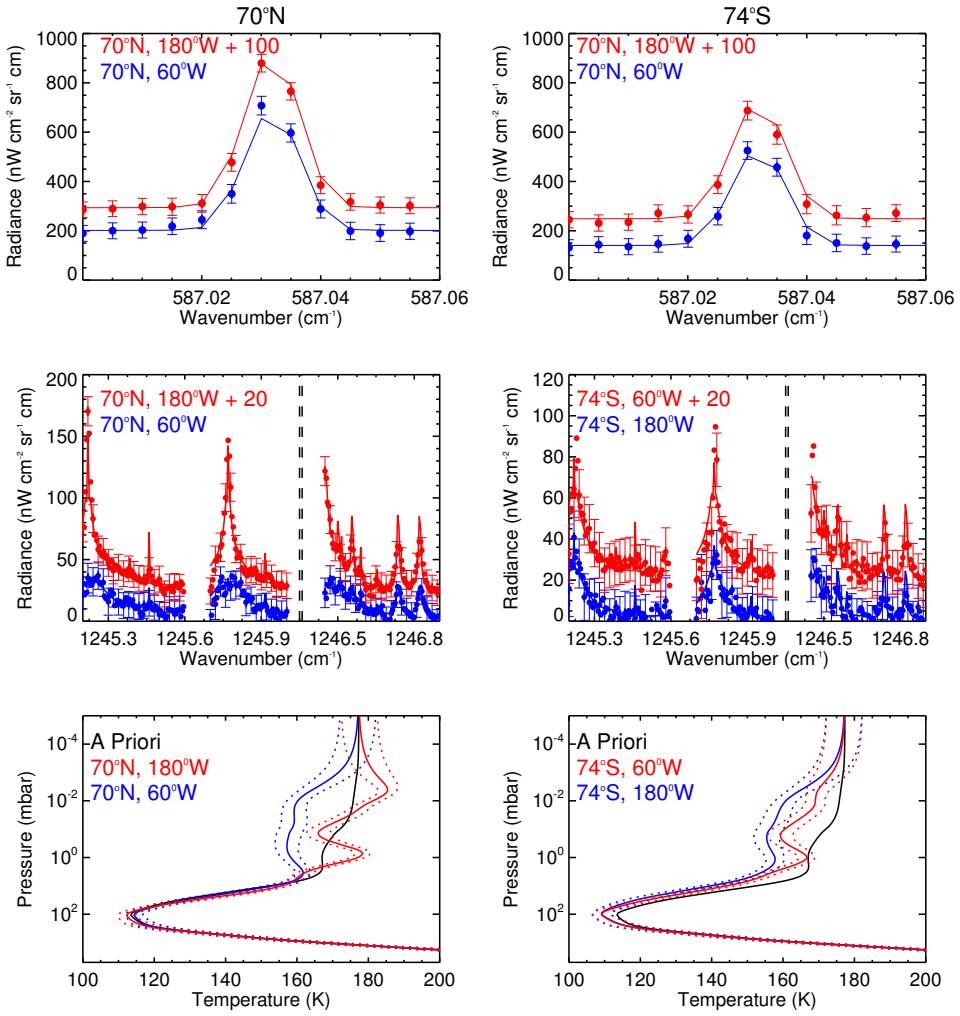

Figure 5: Model-data spectral comparisons of H_2 S(1) emission (top row) and CH_4 emission (2nd row) and the corresponding retrieved vertical profiles of temperature. On the left, results for 70°N, 180°W (on the auroral hotspot) are shown in red, 70°N, 60°W are shown in blue. On the right, results for 74°S, 60°W (on the southern auroral hotspot) are shown in red, for 180°W in blue. The black temperature profile indicates the *a priori* profile.

alternative *a priori*. We performed these additional tests on the spectra at 70°N, 60°W, 72°S, 180°W, which are representative quiescent longitudes in the north and south, and 70°N,180°W and 72°S, 60°W, which respectively cover the northern and southern auroral regions.

Figure 6 shows the temperature *a priori* tested and the corresponding retrieved profiles of temperature. At quiescent longitudes in the north and south, temperatures retrieved from the different *a priori* converge (within 5 K) in the 100- to 0.01-mbar pressure range. At pressures lower than 0.01 mbar, retrieved temperatures tend back to *a priori* values since there is no sensitivity in the measurements at this level. Similarly, the retrieved temperature structure in both northern and southern auroral regions is highly robust from 100 to 0.01 mbar, regardless of which *a priori* profile was used. In both auroral locations, a temperature maximum is retrieved at approximately 1 mbar, a temperature minimum retrieved at approximately the 0.1-mbar level and temperatures rise until the 0.01-mbar level. The retrieved profiles converge on this structure even when the temperature retrieval was started from an *a priori* that was isothermal at a significantly cooler or warmer temperature. Thus, we believe these features of the temperature profile in auroral regions are robust and physical.

4.4. Comparison with Cassini-CIRS

In order to compare the temperature structure retrieved from Cassini-CIRS measurements in 2001 with that retrieved from TEXES in 2014, we chose not to simply compare retrieved temperatures at a single pressure level since the vertical resolutions and sensitivities of the CIRS and TEXES spectra are very different due to their highly different spectral resolving powers. Instead, we chose to compare the observed CIRS radiances with a forward model of the temperature profile retrieved by TEXES but at the spectral resolution and viewing geometry of the CIRS observations. At each latitude and longitude, the retrieved temperature profile from IRTF-TEXES

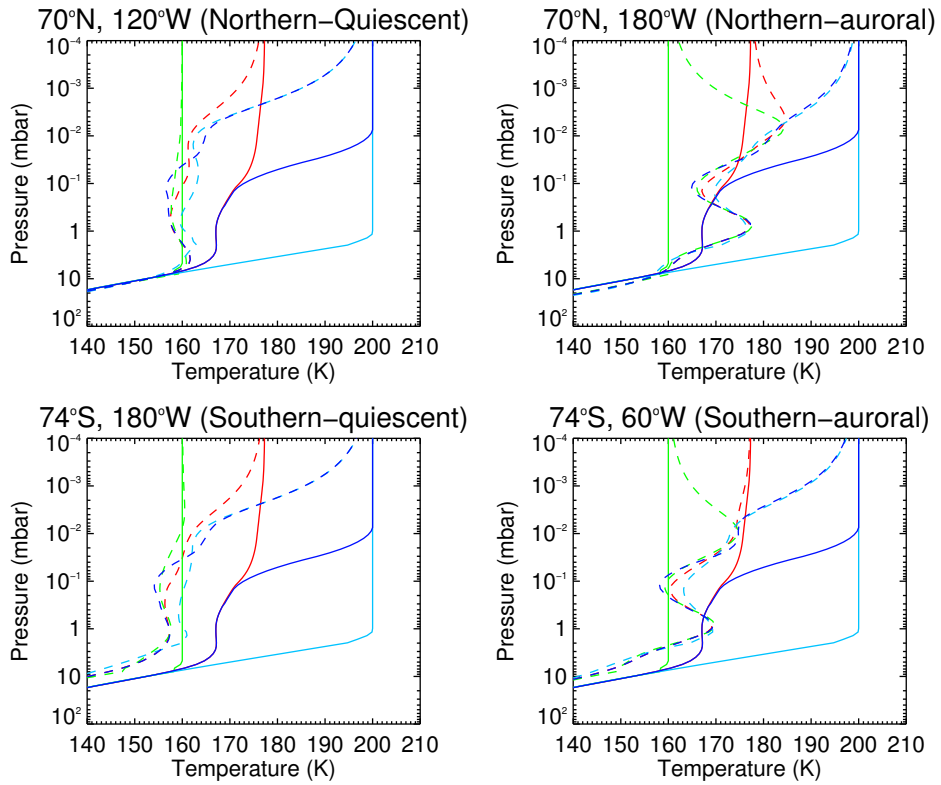

Figure 6: Retrieved vertical profiles of temperature at 70°N (1st row), 60°W (left) and 180°W (right) and 72°S (2nd row), 180°W (left) and 60°W (right) starting from different *a priori* profiles. Solid profiles correspond to the *a priori*, dashed profiles of the same colour show the corresponding retrieved vertical profiles. The results demonstrate that the bifurcated temperature profile in auroral regions is retrieved regardless of the initial *a priori* profile.

spectra was forward-modelled at $\Delta\tilde{\nu} = 2.5$ cm^{-1} spectral resolution and at the same emission angle as the CIRS, ATMOS02A in 2000 spectrum at the same location, where available (see Sinclair et al. (2017a)). Figure 7 compares distributions of the observed CIRS radiances and the forward modelled TEXES radiances and their difference. As shown, there appears to be both morphological differences in CH_4 emission superimposed on an overall systematic offset of radiance, with overall higher radiances measured by CIRS than in TEXES. We discuss the morphological and systematic differences in turn below.

4.4.1. Morphological differences

Temperature results from TEXES show a horizontal extension of warm temperatures west of the main auroral hot spot at 180°W at high-northern latitudes. However, such warmer temperatures are absent in the CIRS radiances with warm temperatures very much localised to the main hotspot region at 180°W. Although this morphological difference appears in a comparison of radiances at the same spectral resolution and emission angle, it is possible that the high vertical resolution provided by TEXES has highlighted a finer scale structure of the temperature profile that cannot be measured by CIRS. We therefore cannot be certain whether the warmer, extended tail of gas west of the northern auroral hotspot in TEXES measurements in 2014 and its absence from CIRS in 2000 indicates a physical evolution between these two years or is an artefact of the spectral resolving power.

The majority of the southern auroral-related hotspot is hidden from view in both TEXES and CIRS measurements due to its position at a comparably higher latitude compared to the northern auroral region. However, the edges of the long-axis of the oval hotspot are visible and can be used to assess the longitudinal orientation of the hotspot feature. In CIRS measurements in 2001, the orientation of the southern auroral oval is approximately 25°/205°W in longitude whereas in TEXES measurements in 2014, the orientation appears to have moved west to approximately 60°/240°. The variable position of the aurorally-heated 1-mbar temperatures associated with the southern aurora has been observed previously (e.g. Caldwell et al. 1988) and remains a puzzle. As we suggested above for the northern auroral region, we suggest the aurorally-warmed gas at the 1 mbar level is subject to horizontal advection.

4.5. Radiance differences

Cassini-CIRS measurements in 2001 measured systematically brighter CH_4 emission with respect to TEXES measurements in 2014, with differences in brightness temperature at 1305 cm^{-1} on the order of 5 - 10 K. While such changes

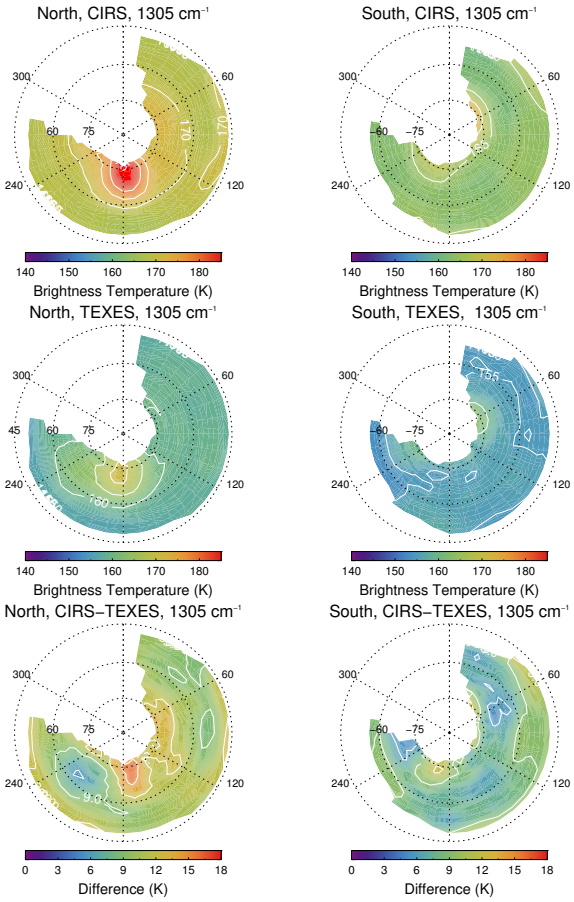

Figure 7: Polar projected distributions in the north (left) and south (right) of observed brightness temperatures in the CH_4 Q branch (1305 cm^{-1} from Cassini-CIRS in 2000 (1st row), forward-modelled brightness temperatures of IRTF-TEXES in 2014 at 2.5 cm^{-1} spectral resolution (2nd row) and the difference (CIRS minus TEXES, 3rd row). This plot demonstrates that a systematic offset as well as morphological differences exist between CIRS measurements in 2001 and TEXES measurements in 2014 of CH_4 emission.

in the brightness temperature of CH_4 emission are of the order previously observed in comparing Voyager-IRIS and Cassini-CIRS measurements in 1979 and 2001, we do not believe the change in solar radiative forcing due to the axial tilt and eccentricity can explain the large offset in CH_4 emission between CIRS and TEXES measurements.(Simon-Miller et al., 2006; Nixon et al., 2007, 2010). We note that Jupiter's subsolar latitude and distance from the Sun changed from 3.3°N and 5.04 AU during the Cassini flyby in January 2001 to 0.26°N and 5.31 AU during the TEXES measurements in December 2014. We would therefore expect warmer temperatures in the northern hemisphere and cooler temperatures in the southern hemisphere in 2001 compared to 2014 yet there are comparable differences in CH_4 emission between CIRS and TEXES in both hemispheres (Figure 7).

We also note a contrast in the solar activity during the Cassini flyby in 2001 and the TEXES measurements in 2014 (Figure 8).

While Cassini-CIRS measurements in 2001 and IRTF-TEXES measurements in 2014 both captured Jupiter during periods of solar maxima, the solar activity (in terms of the monthly-mean sunspot number) was a factor of 2 higher in 2001 compared to 2014. In the next Section, we compare the TEXES and CIRS observations at 70°N, 60°W and 70°N, 180°W to determine whether the change in solar activity corresponds to a change in the temperature contrast between quiescent locations and the northern auroral hotspot. However, we do not believe the difference in solar activity between 2001 and 2014 can explain the overall offset in CH_4 emission and therefore stratospheric temperatures between these dates. While the short-wave radiation varies by a factor of 2 to 3 over the course of the solar cycle (Moses and Greathouse, 2005), the wavelength-integrated solar output varies by less than 1%. In addition, the CH_4 emission sounds the 1-mbar level, where radiative lifetimes are comparable with the length of a Jupiter year (Conrath et al., 1990) and the ~11-year period of the solar cycle. Thus, 1-mbar temperatures would not be expected to vary due to radiative effects over a ~10-year time period.

Instead, we attribute the differences in brightness temperature between the CIRS and TEXES measurements to a radiometric calibration issue. We believe this issue is a systematic one and therefore should not affect relative latitudinal and longitudinal variations. Fouchet et al. (2016) found similar offsets in comparing temperatures derived from Cassini-CIRS and IRTF-TEXES measurements of Saturn, which they attributed to terrestrial atmospheric smearing of the beam measured by the telescope. We suggest that a similar issue is present in the TEXES observations presented in this work. We also find that the radiometric calibration of TEXES measurements is highly consistent (within 10%) night-to-night (Fletcher et al., 2016) and so this systematic offset should also not affect the qualitative interpretation of any variability observed between different dates.

4.6. Auroral-quiescent contrasts

Figure 8 shows the monthly-mean sunspot number as a measure of the solar activity. As shown, the years 2000 and 2014 both correspond to periods of solar maxima. However, the magnitude of solar activity, at least in terms of the monthly-averaged sunspot number visible on the solar disk, is almost a factor of 2 higher in 2001 compared to 2014. Thus, a comparison of stratospheric temperatures in auroral regions between 2000 and 2014 could indicate if and by how much the auroral-related heating in the stratosphere is affected by the magnitude of solar activity. If there is evolution of temperature over this timescale, it might imply that auroral heating in the stratosphere is directly affected by the input of charged particles in the thermosphere. Any absence of evolution may suggest the auroral-related heating at the 1-mbar level is driven by processes which act on timescales longer than the ~11 year solar cycle.

[1] https://solarscience.msfc.nasa.gov/greenwch/SN_m_tot_V2.0.txt

However, the apparent systematic offset in radiances between CIRS and TEXES (Section 4.5) makes the comparison of absolute temperatures derived in 2001 and 2014 obsolete. Instead, we have compared the relative contrast in CH_4 emission between auroral and quiescent longitudes, which allows for any radiometric offsets to be removed. Figure 9 compares the observed CIRS radiances in 2000 at 70°N, 60°W and 180°W, forward models of the TEXES results at these locations and the ratio of radiance in these two locations. This ratio effectively describes the contrast in CH_4 emission between the main auroral hotspot and a representative quiescent location in the same latitude band. As shown, both CIRS measurements in 2001 and TEXES measurements in 2014 indicate that Q-branch, CH_4 emission (~1305 cm^{-1}) was approximately 2.3 times brighter at 70°N, 180°W compared to 60°W. However, TEXES measurements show P-branch CH_4 emission (1250 to 1280 cm^{-1}) to be up to 1.6 times brighter at 70°N, 180°W compared to 60°W whereas CIRS measurements show the contrast only to be as high as 1.5. The fact that the auroral-quiescent contrast in TEXES measurements in 2014 was higher than the contrast indicated in CIRS measurements and the fact that the latter was measured during a period of higher solar activity might suggest 1-mbar temperatures in the auroral region are uncorrelated with solar activity. However, we note that Kostiuk et al. (2016) show a correlation of the magnitude of C_2H_6 emission with solar activity using a long-term record of ground-based observations from 1979 to 2016. In order to make any conclusions about the variability of temperatures in Jupiter's auroral regions, we require measurements from a consistent dataset at a higher temporal cadence over a longer time period. The variability of Jupiter's aurora will be addressed in future publications using TEXES spectra measured on different dates.

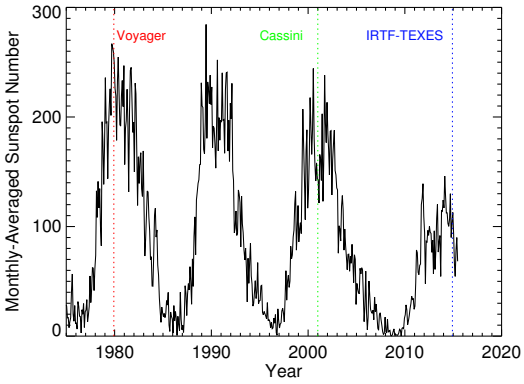

Figure 8: The monthly-averaged sunspot number[1] over time, as an indicator of solar activity. The dates marking the Voyager and Cassini flybys and the dates of the IRTF-TEXES measurements (presented in this work) are indicated by the vertical dotted lines.

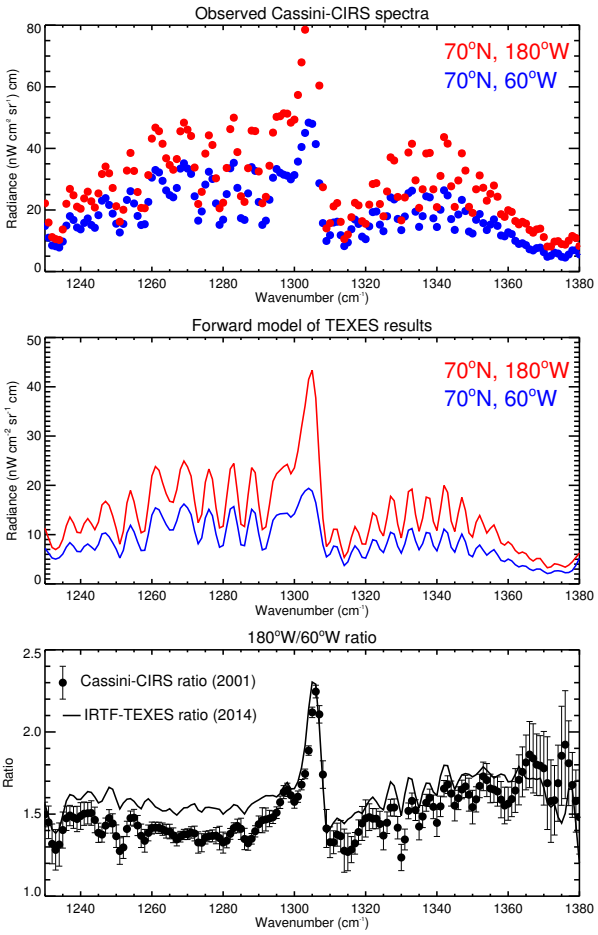

Figure 9: The observed Cassini-CIRS radiances (top plot) in the CH_4 band at 70°N, 60°W (blue points with error bars) and 70°N, 180°W (red points with error bars). The middle plot shows forward models of the retrieved temperatures at 70°N, 60°W (blue) and 70°N, 180°W at the same spectral resolution and emission angle as the Cassini-CIRS observations in these locations. The bottom plot shows the ratio of the radiance at 70°N, 60°W and 70°N, 180°W in the observed CIRS radiances (points with error bars) and the forward model of the TEXES results (solid line). This demonstrates that the contrast in CH_4 emission between 70°N, 180°W (the northern auroral hotspot) and 70°N, 60°W (a quiescent location) was larger in 2014 than 2001.

5. C_2H_2, C_2H_4, C_2H_6 results

The vertical profiles of C_2H_2, C_2H_4 and C_2H_6 were retrieved from their emission features in the 730 cm^{-1}, 950 cm^{-1} and 819 cm^{-1} settings respectively. The vertical profile of C_2H_2 was retrieved from 728.9 - 729.25 cm^{-1}, 729.4 - 729.8 cm^{-1} and 730.3 - 730.6 cm^{-1}, the vertical profile of C_2H_4 was retrieved from the 949.3 - 949.4 cm^{-1}, 949.425 - 949.9 cm^{-1} and 950.05 - 950.4 cm^{-1} and the vertical profile of C_2H_6 was retrieved from the 818.85 - 819.4 cm^{-1}, 819.5 - 819.9 cm^{-1}, 821.0 - 821.3 cm^{-1} and 822.2 - 822.6 cm^{-1} spectral ranges. These wavenumber ranges were chosen in order to capture a mixture of weak and strong emission lines of each species whilst avoiding gaps in the instrument's spectral coverage. At each

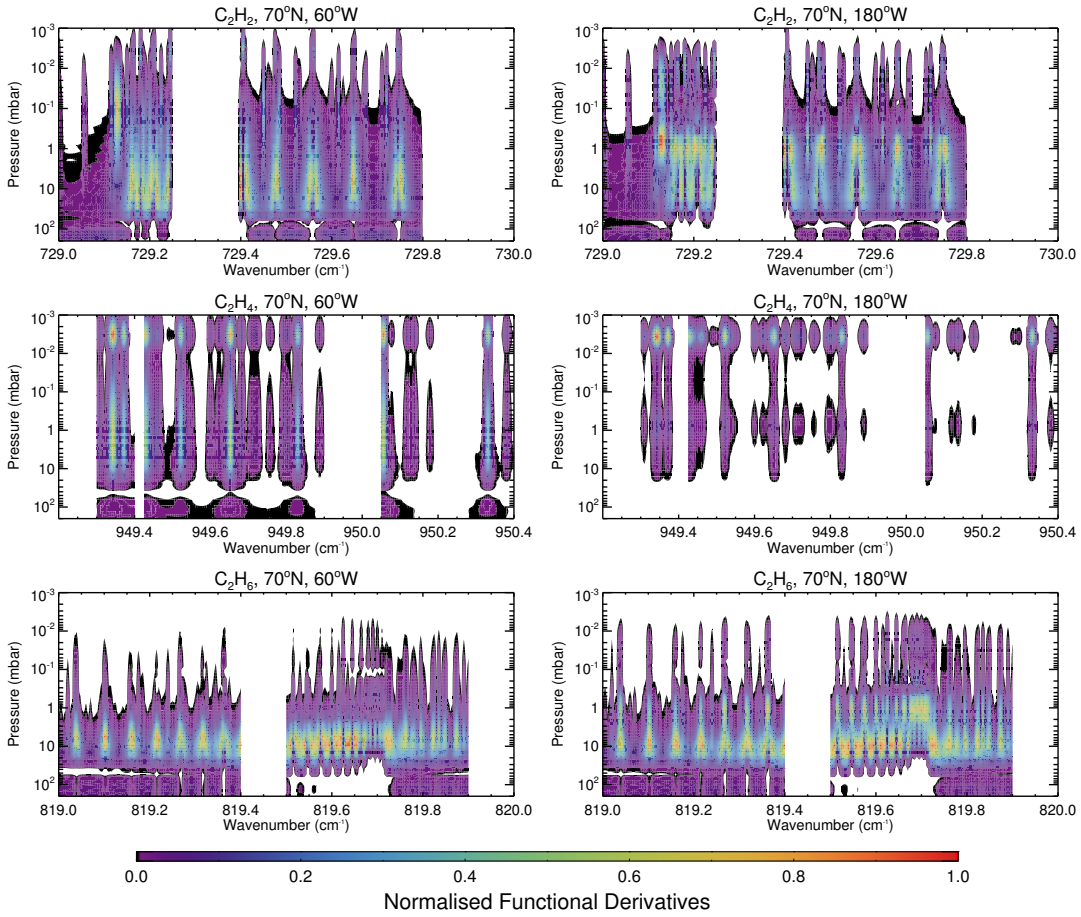

Figure 10: The absolute, normalised, vertical functional derivatives at 70°N, 60°W (left) and 70°N, 180°W (right) for C_2H_2 in the 730 cm^{-1} setting (top), C_2H_4 in the 950 cm^{-1} setting (middle) and C_2H_6 in the 819 cm^{-1} setting (bottom).

latitudinal and longitudinal location, the vertical temperature profile and uncertainty retrieved previously (Section 4) was adopted into the atmospheric model. Initially, we adopted the reference vertical profiles of C_2H_2, C_2H_6 and C_2H_4, based on the model results by Moses et al. (2005), as the *a priori* profiles for each hydrocarbon.

5.1. Vertical sensitivity

Figure 10 compares the vertical functional derivatives with respect to C_2H_2, C_2H_4 and C_2H_6 at 70°N, 60°W and 70°N, 180°W as representative examples of the vertical sensitivity in quiescent and auroral locations respectively. The 730 cm^{-1} setting provides sensitivity to C_2H_2 from approximately 10 mbar to 0.01 mbar, with greater sensitivity to lower pressures in auroral conditions. Similarly, the sensitivity to C_2H_4 in nominal temperature conditions in the 950 cm^{-1} setting exhibits two peaks at the 1-mbar level and the 10-µbar level. In auroral conditions, the sensitivity to C_2H_4 greatly increases at the 10-µbar level while decreasing at the 1-mbar level. However, there is negligible difference in the sensitivity to C_2H_6 in the 819 cm^{-1} between quiescent and auroral conditions, with the greatest sensitivity to C_2H_6 exhibited in the 5- to 1-mbar level.

5.2. Retrieved distributions

Figure 11 and 12 show the polar distributions of retrieved C_2H_2, C_2H_4 and C_2H_6 concentrations at four different stratospheric altitudes. In the northern auroral region, our results indicate that C_2H_2 and C_2H_4 are enriched with respect to quiescent longitudes. Unlike the enhancement in temperature, which appeared approximately centred within the auroral oval, the highest concentrations of C_2H_2 and C_2H_4 are off-centre and closer to the western edge of the northern oval. It is uncertain whether this is a physical effect or perhaps an artefact of the spatial resolution. In the northern auroral region, C_2H_6 appears enriched at the 5 mbar level but depleted at pressures lower than 1 mbar, however, as we show in Section 5.6, these changes are not significant with respect to uncertainty. In the southern auroral region, C_2H_4 is also enriched within the southern auroral region whereas C_2H_2 and C_2H_6 do not exhibit any noticeable change in this region. We investigate these observed behaviours further in the following sections.

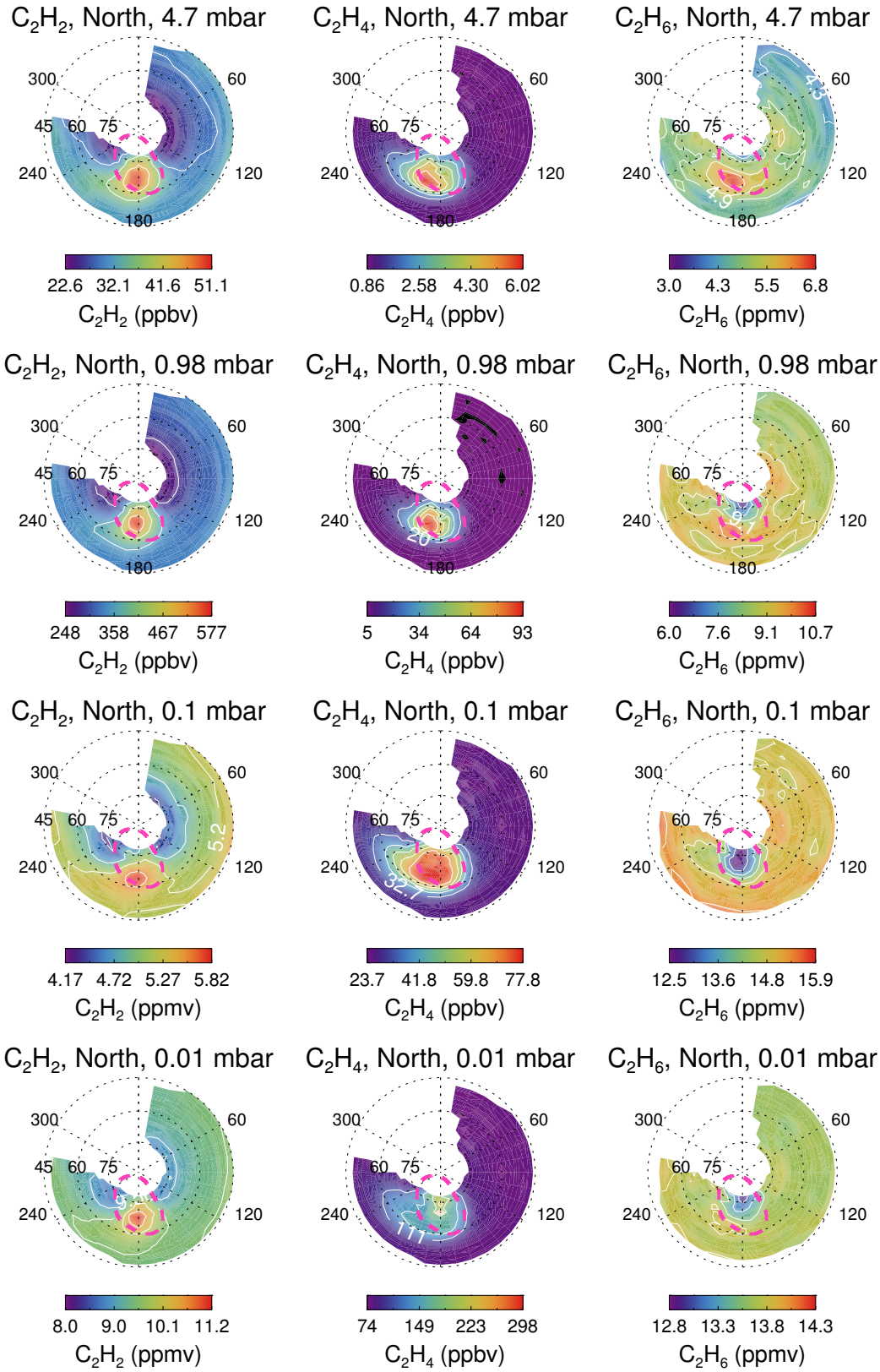

Figure 11: North polar distributions of retrieved C_2H_2 (left), C_2H_4 (middle) and C_2H_6 (right) at 4.7 mbar (top row), 0.98 mbar (2nd row), 0.1 mbar (3rd row) and 0.01 mbar (4th row). The concentrations are coloured according to the colourbar indicated under each plot.

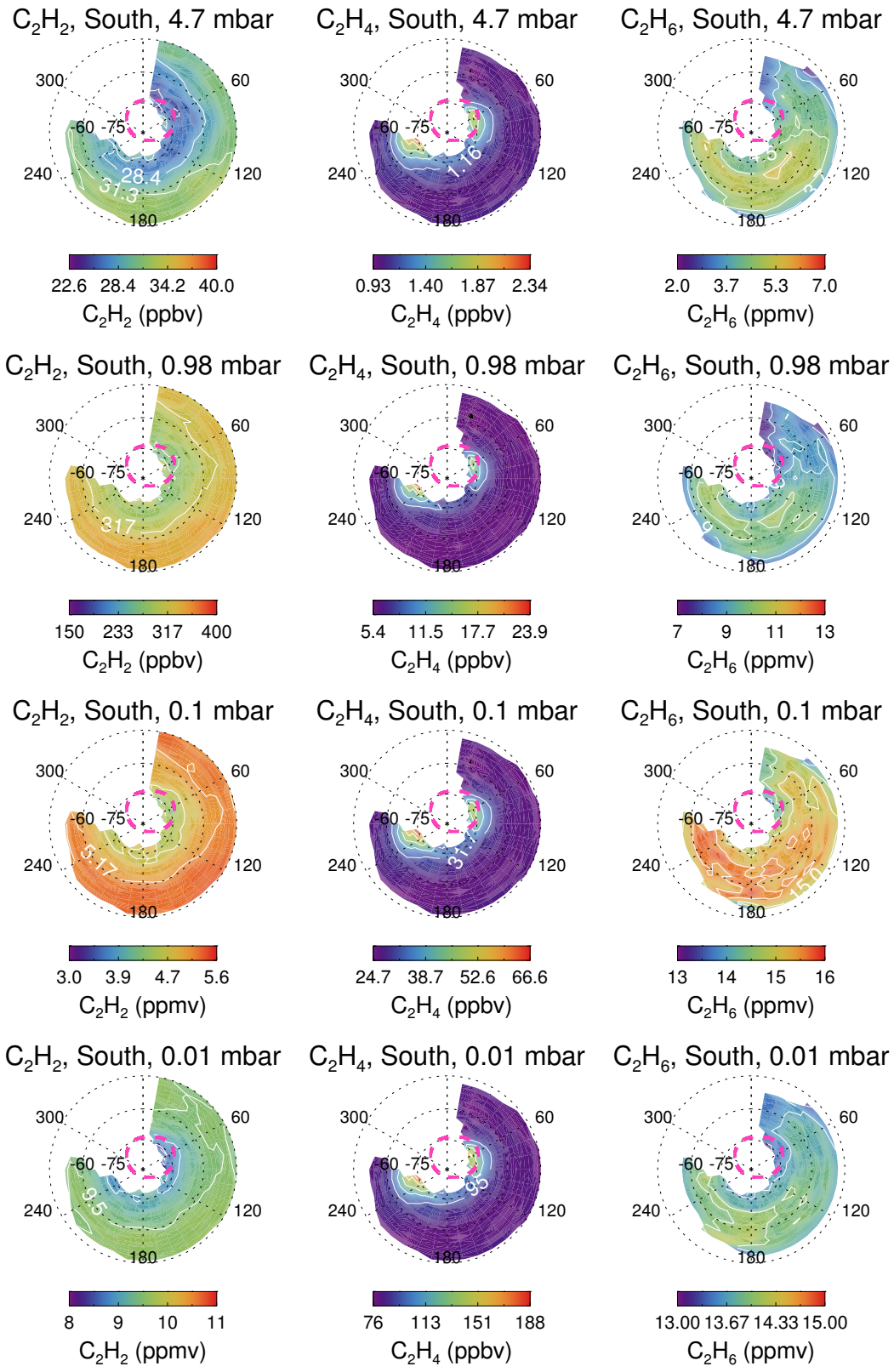

Figure 12: South polar distributions of retrieved C_2H_2 (left), C_2H_4 (middle) and C_2H_6 (right) at 4.7 mbar (top row), 0.98 mbar (2nd row), 0.1 mbar (3rd row) and 0.01 mbar (4th row). The concentrations are coloured according to the colourbar indicated under each plot.

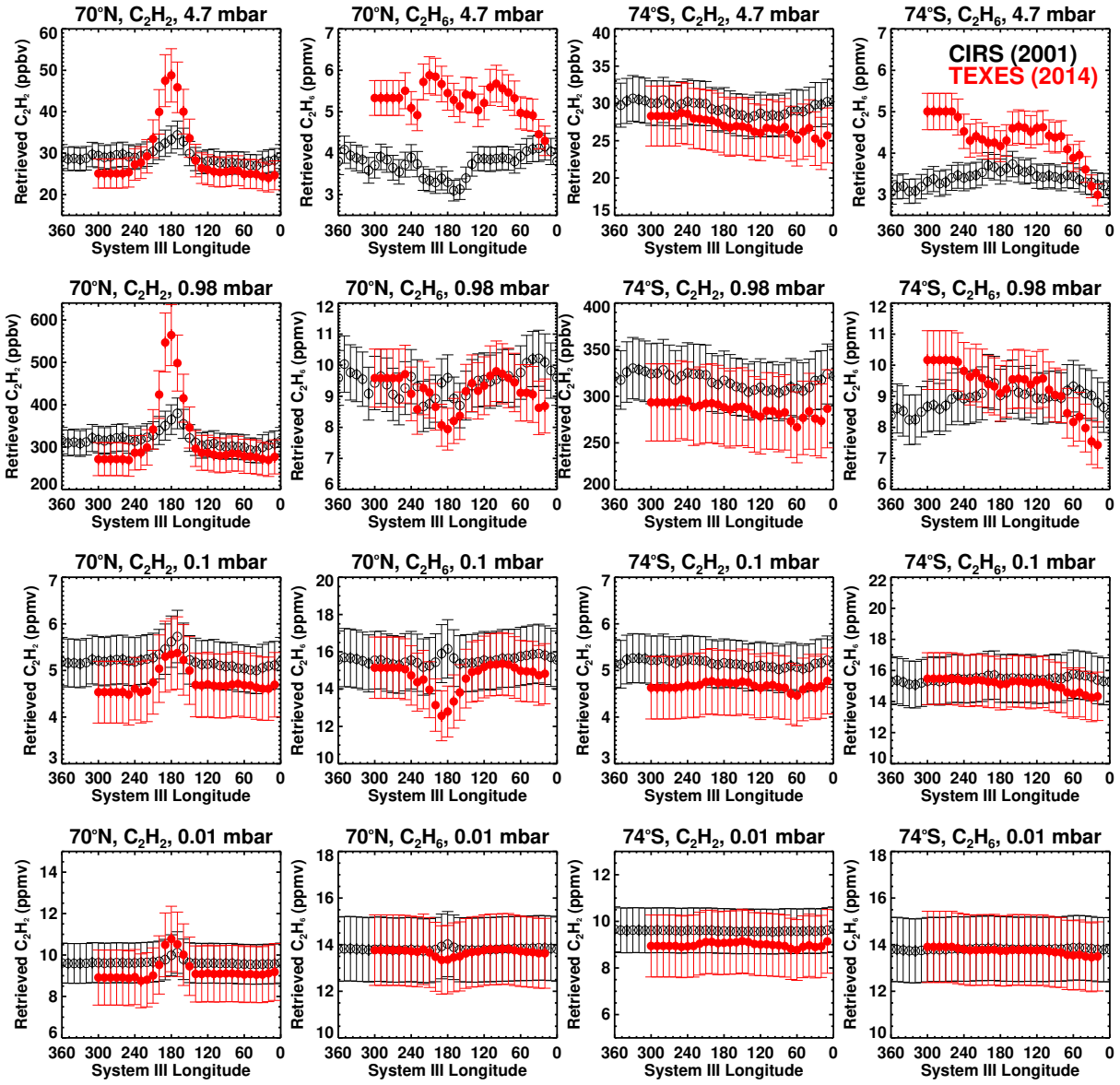

Figure 13: The retrieved concentrations of C_2H_2 and C_2H_6 from TEXES (red results) as a function of longitude at 70°N (1st and 2nd columns) and 74°S (3rd and 4th columns). Results are shown at four different pressures levels: 4.7 mbar (top row), 0.98 mbar (2nd row), 0.1 mbar (3rd row) and 0.01 mbar (4th row). Note that C_2H_2 results are quoted in ppbv at 4.7 and 0.98 mbar but quoted in ppmv at 0.1 mbar and 0.01 mbar. For comparison, the results from Cassini-CIRS (Sinclair et al., 2017a) are shown in black. We have not compared results for C_2H_4 since there was poor constraint on its concentration at the limited spectral resolution of Cassini-CIRS spectra.

5.3. Comparison with Cassini-CIRS

5.3.1. Results at 70°N, 74°S

Figure 13 compares the retrieved concentrations of C_2H_2 and C_2H_6 from TEXES at 70°N and 74°S (the latitude bands containing the northern and southern auroral regions) with those from Cassini-CIRS in 2001 (Sinclair et al., 2017a). Concentrations of C_2H_2 retrieved from IRTF-TEXES and Cassini-CIRS are in agreement within uncertainty outside the auroral regions whereas TEXES results indicate richer concentrations of C_2H_2 inside the northern auroral region from 5 to 1 mbar. As shown in tests of forward models in Section 5.3.2, this discrepancy between CIRS and TEXES results cannot be explained by the very different spectral resolutions (and therefore vertical sensitivity) of the two datasets. Thus, we believe there were indeed richer concentrations of C_2H_2 within the northern auroral region in December 2014 compared to January 2001. Retrieved concentrations of C_2H_6 from IRTF-TEXES and Cassini-CIRS observations are also consistent within uncertainty) at quiescent longitudes at the 1 mbar level, however, at 5 mbar, concentrations retrieved TEXES in 2014 are richer than those from Cassini-CIRS. As shown in Section 5.3.2, this discrepancy can be explained by the difference in spectral resolution,

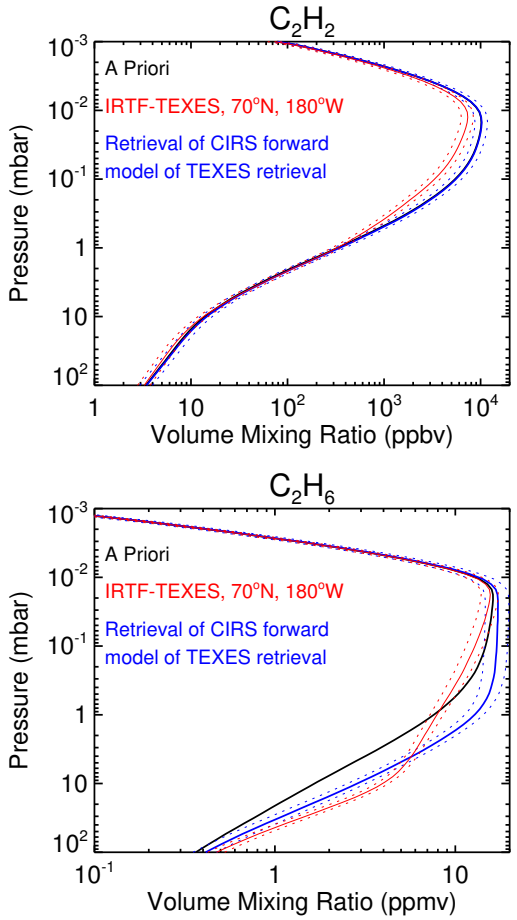

Figure 14: Retrieval tests of the vertical profiles of C_2H_2 (top) and C_2H_6 (bottom) at 70°N, 180°W by synthetic Cassini-CIRS spectra. Black profiles show the *a priori*, red profiles indicate the result retrieved from TEXES observations, which were adopted in the computation of the synthetic CIRS spectra. The blue profiles indicate the vertical profile retrieved from the synthetic CIRS spectrum. In summary, differences in the spectral resolution between CIRS and TEXES spectra, and therefore their vertical sensitivity, can explain the lower abundances of C_2H_6 retrieved at 4.7-mbar by the former.

and therefore vertical sensitivity, of the Cassini-CIRS and IRTF-TEXES observations. At pressures of 0.1 mbar and 0.01 mbar, the concentrations of C_2H_2 and C_2H_6 retrieved from Cassini-CIRS and IRTF-TEXES are also in agreement within error bars. However, there is comparably much less sensitivity to both hydrocarbons at these pressures, in particular to the CIRS measurements (see Figure 5 of Sinclair et al. (2017a)). Thus, the apparent agreement of CIRS and TEXES results at these pressures simply results from retrieved values tending back to the same *a priori* profile.

5.3.2. Forward model tests

We performed forward modelling tests to determine to what extent differences in the CIRS and TEXES results could be explained by their differing spectral resolutions and therefore vertical resolutions and sensitivity to atmospheric parameters. Adopting the vertical profiles of temperature, C_2H_2 and C_2H_6 retrieved by TEXES at 70°N, 180°W, spectra were forward-modelled at 2.5 cm^{-1} and at an emission angle of 70° in order to simulate a high-emission angle Cassini-CIRS observation. Noise consistent with the observed CIRS spectrum at the same latitude/longitude in Sinclair et al. (2017a) was added to simulate an observation. The temperature profile and uncertainty retrieved by TEXES at this location were adopted in the atmospheric model and the vertical profiles of C_2H_2 and C_2H_6 were retrieved from the synthetic CIRS spectrum.

Figure 14 shows the results of these tests. The retrieval of the vertical profile of C_2H_2 from the synthetic CIRS spectrum matches the true result retrieved by TEXES from 10 to 1 mbar with less agreement expected at lower pressures due to the lack of sensitivity by CIRS measurements to these pressures. However, the vertical profiles retrieved by TEXES and the synthetic CIRS spectra are in disagreement. Retrieval of C_2H_6 from CIRS indicates an enrichment by a smaller magnitude over a larger pressure range and therefore underestimates the concentration of C_2H_6 at pressures higher than 2 mbar. We conclude this accounts for the lower concentrations of C_2H_6 retrieved from CIRS, with respect to IRTF-TEXES, at 4.7 mbar (Figure 13).

5.4. C_2H_2

Figure 15 shows model-data spectral comparisons of C_2H_2 and the corresponding vertical profiles at 70°N, 60°W and 180°W. The enrichment of C_2H_2 in the northern auroral region with respect to quiescent longitudes occurs at pressures higher than 0.3 mbar, with differences in concentration at pressures lower than this level being insignificant with respect to uncertainty. For example, at the 1-mbar level, C_2H_2 increases from 278.4 ± 40.3 ppbv at 70°N, 60°W to 564.4 ± 72.0 ppbv at 70°N, 180°W: an increase of 286.0 ± 82.5 ppbv or approximately 30%. This enrichment is further indicated by the dashed, red line in the top plot of Figure 15, which shows a forward modelled spectrum using the temperature profile retrieved at 70°N, 60°W but the retrieved C_2H_2 profile at 70°N, 180°W. The concentration of C_2H_2 retrieved in the northern auroral hotspot yields radiances that greatly overestimate the strength of the C_2H_2 lines at 70°N, 60°W.

We note that the fit to the cores of the strong C_2H_2 lines in the spectrum at 70°N, 180°W is very poor. As shown in Figure 16, we attempted to improve the fit to the cores of these lines by performing further retrievals with different *a priori* and approaches. The cores of these lines probe the upper stratosphere at pressures lower than 10^{-2} mbar (Figure 10). While starting retrievals from *a priori* with richer concentrations at higher altitudes marginally improves the fit within the cores of the C_2H_2 lines at 729.54 and 729.74 cm^{-1}, the fit to the weaker C_2H_2 lines at 729.44, 729.61 and 729.72 cm^{-1} substantially deteriorates (see green and orange spectra in top plot of Figure 16). We also performed a simultaneous retrieval of temperature and C_2H_2 in order to check whether a

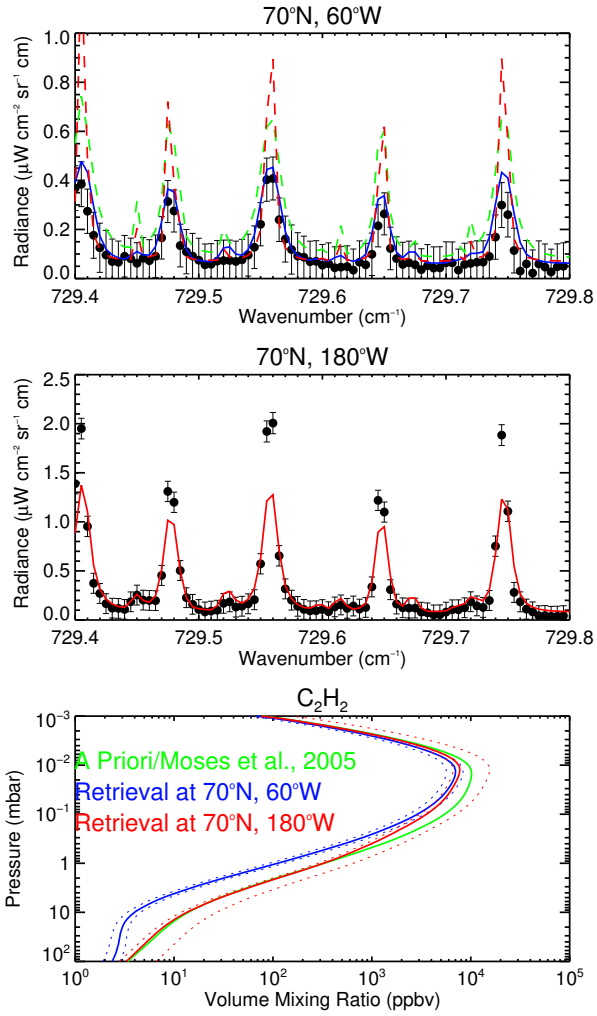

Figure 15: Model-data spectral comparisons for 70°N, 60°W (a representative quiescent location) and 70°N, 180°W (the northern auroral hotspot) are shown in the top and middle plots respectively. Points with error bars represent observed TEXES spectra and solid lines indicate modelled spectra associated with the retrieved vertical profiles of C_2H_2 of the same colour shown in the bottom plot. In the top plot, we also show forward modelled spectra (as dashed lines) using the *a priori* vertical profile of C_2H_2 (green) and the vertical profile of C_2H_2 retrieved at 70°N, 180°W (red) in order demonstrate these vertical profiles are too rich in concentration to fit the observed spectra.

change to the temperature profile retrieved from the 587 cm^{-1} and 1248 cm^{-1} (Section 4) would allow a better fit to the C_2H_2 line cores. While this approach does yield the best fit to the line cores, with respect to the other retrieval approaches, the fit to the weaker C_2H_2 features is the poorest.

We believe the inability to fit the cores of the strong C_2H_2 lines demonstrates the presence of strong non-LTE (local thermodynamic equilibrium) emission in these spectral regions in the northern auroral region. The cores of the strong C_2H_2 lines probe pressures lower than 10^{-2} mbar. At these altitudes, the thermal collisional timescale becomes comparable or longer than the spontaneous radiative lifetime, which signifies where the frequency of thermal collisions is not sufficient to resupply the energy lost by spontaneous emission (López-Puertas and Taylor, 2001). The radiative transfer code used for forward modelling and retrievals in this work - NEMESIS - assumes local thermodynamic equilibrium conditions and thus does not parameterise this effect, leading to underestimated radiances in the C_2H_2 line cores. Non-LTE parameterisations may be included in NEMESIS in the future but this work is beyond the scope of this work.

5.5. C_2H_4

C_2H_4 is enriched in the northern auroral region with respect to quiescent longitudes. For example, the concentration of C_2H_4 at the 5 μbar level increases from 0.669 ± 0.129 ppmv at 70°N, 60°W to 6.509 ± 0.811 ppmv at 70°N, 180°W. At 72°S, the enrichment of C_2H_4 is less significant with respect to longitude: increasing at the 5 μbar level from 1.548 ± 0.278 ppmv at 72°S, 180°W to 2.601 ± 0.457 ppmv at 72°S, 60°W. Nevertheless, the magnitude of these 5-μbar concentrations are over a factor of 2 higher than the ~0.75 ppmv predicted by Moses et al. (2005) for a mid-latitude (37°N) despite the fact that the latter receives more sunlight per jovian year. This demonstrates that an additional source of C_2H_4 besides neutral photochemistry is required to explain these concentrations at high latitudes: as outlined in Sinclair et al. (2017a), we believe ion-neutral chemistry associated with the aurora greatly increases the production of unsaturated hydrocarbons such as C_2H_2 and C_2H_4.

Figure 17 shows model-data spectral comparisons and the vertical profiles of C_2H_4 retrieved in the northern and southern auroral regions and representative quiescent longitudes in the same latitude bands. The enrichment of C_2H_4 in the northern auroral region with respect to 70°N, 60°W in the same latitude band is further demonstrated by the forward model shown in dashed-blue in the middle-left plot, which was computed using the temperature-pressure profile retrieved at 70°N, 180°W (the northern auroral region) but the retrieved vertical profile of C_2H_4 at 70°N, 60°W (a quiescent longitude). As shown, the forward-modelled radiances do not match the observed radiances within the 1-σ level, which shows that an increase in C_2H_4 is indeed required to fit the C_2H_4 emission features. In contrast, a similar comparison at 72°S shows that the vertical profile of C_2H_4 retrieved at 72°S, 180°W, forward-modelled using the temperature-pressure profile retrieved at 72°S, 60°W can generally fit the observed radiances within the 1-σ level. Thus, we conclude that the variations in C_2H_4 between the southern auroral and quiescent regions are negligible, at least at 72°S.

We note that the fits to the cores of the C_2H_4 lines in the northern and southern auroral regions are well-matched by the modelled spectra. This is in contrast to the C_2H_2 model spectra (Section 5.4), where modelled radiances could not fit both the weak C_2H_2 and the cores of the strong C_2H_2 features simultaneously. We attributed this effect in the C_2H_2 spectra

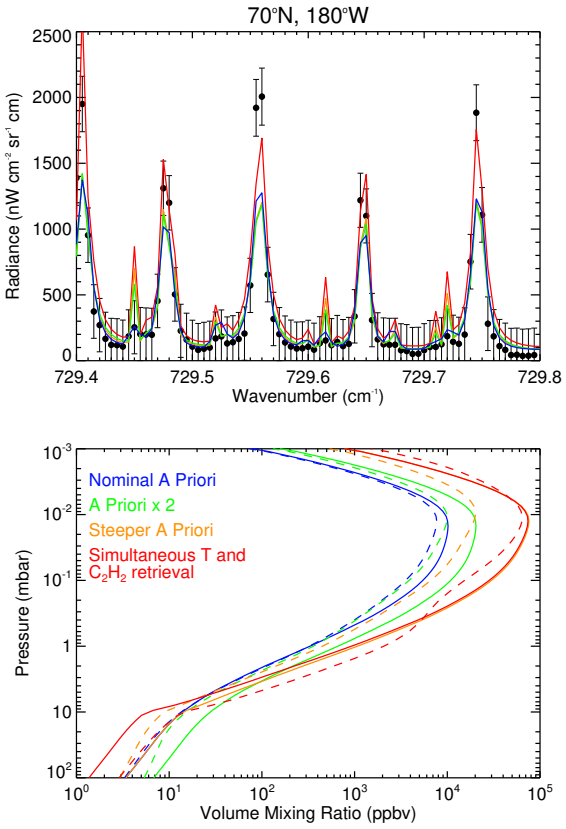

Figure 16: In the top plot, black circles and error bars show the observed radiances in the 730 cm^{-1} at 70°N, 180°W. Solid, coloured lines show the spectra corresponding to the vertical profiles of C_2H_2 shown in the bottom plot of the same colour. As shown, various retrieval and forward model approaches struggle to fit the cores of the strong C_2H_2 lines (e.g. 729.55 cm^{-1}) and the weaker C_2H_2 features (e.g. 729.45 cm^{-1}) simultaneously with the same vertical profile of C_2H_2. We believe this demonstrates the presence of non-LTE emission in the cores of the strongest C_2H_2 lines as discussed in the text.

to be the result of non-LTE emission present in the cores of the strong C_2H_2 lines. The fact that we can fit the observed C_2H_4 line strengths readily is suggestive of one or both of the following. Either non-LTE processes affect C_2H_4 molecules relatively less compared to C_2H_2. Or there is indeed non-LTE emission present in the cores of the C_2H_4 emission features, however, the C_2H_4 line strengths are more comparable across the 950 cm^{-1} spectral setting and so the retrieval can fit the line cores by increasing the abundances of C_2H_4 in the 1- to 10-µbar level. We note that the retrieved vertical profile of C_2H_4 at 70°N, 180°W does exhibit a larger vertical gradient, with higher abundances of C_2H_4 at the 5 µbar level, compared to quiescent longitudes. It is unclear whether this is physical, resulting from increased production of C_2H_4 in the upper stratosphere in the auroral region or due to fitting of the non-LTE emission as described above.

5.6. C_2H_6

While Figure 11 shows the northern auroral hotspot to be enriched in C_2H_6 at the 5-mbar level and depleted at pressures of 1 mbar and lower, we find these longitudinal variations in C_2H_6 to be insignificant with respect to uncertainty. For example, at the 1 mbar level, we retrieve concentrations of 9.03 ± 0.98 ppmv at 70°N, 60°W and 7.66 ± 0.70 ppmv at 70°N, 180°W, which are in agreement within the 1-σ level. This is also demonstrated in Figure 18, which shows model-data spectral comparisons in the northern and southern auroral hotspots and representative quiescent locations in the same latitude bands. Nevertheless, a lower retrieved concentration of C_2H_6 within the northern and southern auroral hotspots, with respect to quiescent longitudes, is qualitatively consistent with our analysis of Cassini-CIRS observations presented in Sinclair et al. (2017a). We believe this demonstrates that C_2H_2 and C_2H_4 are converted into C_2H_6 by sequentail H-atom addition outside the auroral region, thus enriching the concentrations of C_2H_6 in quiescent longitudes.

6. Discussion

6.1. Temperature

The temperature structures retrieved from Cassini-CIRS measurements in 2001 and IRTF-TEXES measurements in 2014 agree qualitatively. While the magnitude of retrieved temperatures differ, TEXES also indicates that the majority of auroral-related heating exists in two discrete pressure regions at approximately 1 mbar and 10 µbar. As we discussed in Sinclair et al. (2017a), the fact these two regions are physically separated implies the mechanisms responsible for heating at each level are different, albeit auroral-related. We believe heating at pressures of 10 µbar and lower results directly from the precipitation of charged particles of the magnetosphere. We believe the warmer auroral temperatures at the 1-mbar level result either from heating of auroral haze particulates by absorption of short-wave radiation and/or precipitation of a higher-energy population of charged particles. The influx of charged particles into the upper atmosphere of Jupiter is thought to greatly increase the rates of ion-neutral chemistry, which leads to higher production rates of benzene (C_6H_6, an aromatic hydrocarbon) and polycyclic aromatic hydrocarbons or PAHs (Friedson et al., 2002; Wong et al., 2003). These PAHs then form the building blocks that lead to the production of haze particles. A chemistry model of this mechanism for haze formation does predict the highest number densities of haze particles at approximately the 1-mbar level (Wong et al., 2003) though Zhang et al. (2015) show the heating effect to be highest at the 10-mbar level instead. In future work, we seek to measure the temporal variability of 1-mbar temperatures as a test of which of the aforementioned mechanisms is responsible for the 1-mbar heating. Variability of 1-mbar temperatures on the timescale of half a Jupiter year (~ 6 years), as the subsolar latitude varies, would be suggestive of solar heating of haze particles. More rapid variability on timescales shorter than 1

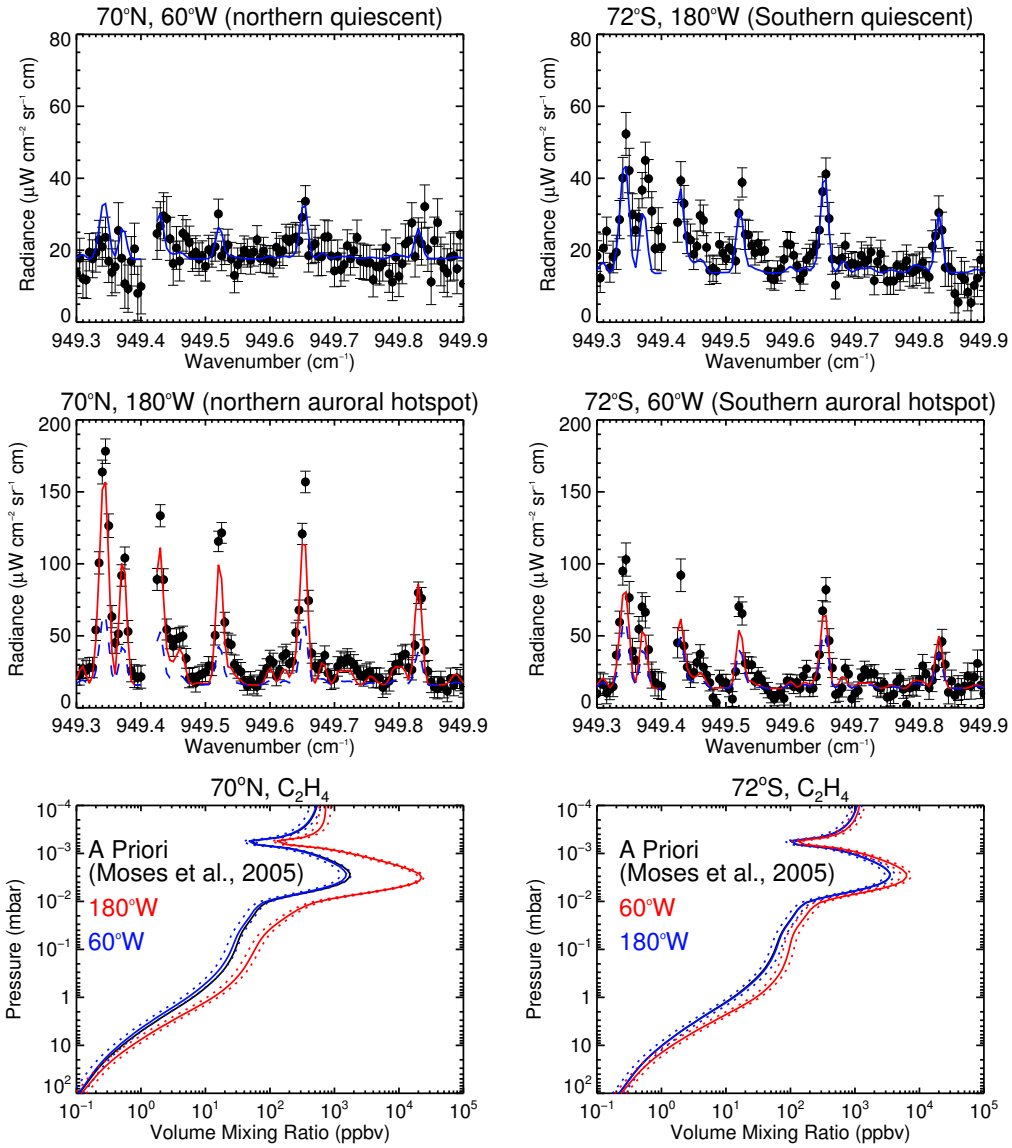

Figure 17: Model-data spectral comparisons at quiescent locations in the north (top, left) and south (top, right), the northern auroral hot spot (middle, left) and southern auroral hotspot (middle, right). Observed spectra are shown as points with error bars while modelled spectra are shown as coloured, solid lines. The corresponding retrieved vertical profiles of C_2H_4 are shown as solid lines of the same colour in the bottom plots and the 1-σ retrieval uncertainty is indicated by dotted lines of the same colour. The solid, black profile shows the vertical profile of C_2H_4 predicted by Moses et al. (2005), which was adopted as the *a priori* profile in the retrievals.

(Earth) year would be more suggestive of a charged particle precipitation source, which is modulated by the solar wind dynamical pressure at Jupiter.

6.2. C_2H_2, C_2H_4, C_2H_6

At high-northern latitudes, we find that C_2H_2 and C_2H_4 are enriched within the northern auroral region with respect to quiescent longitudes whereas C_2H_6 exhibits no significant change (with respect to uncertainty) over the same longitude range. At high-southern latitudes, uncertainties on retrieved concentrations of C_2H_2, C_2H_4 and C_2H_6 are similarly larger than their longitudinal variation, which prevents us from making statistically-significant conclusions of how they are modified by the auroral region at high-southern latitudes. In addition, the southern auroral region is situated at a comparably higher latitude compared to the northern auroral region. Thus, the poorer visibility of the southern auroral region may also be a factor in finding negligible longitudinal variations at these high-southern latitudes.

Nevertheless, the behaviour of C_2H_2 at high-northern latitudes is consistent with our discussion of the effects of the ion-neutral chemistry on the neutral hydrocarbon abundances presented in Sinclair et al. (2017a). By analogy with ion-neutral chemistry models that have been developed for Titan (Vuitton et al., 2007, 2008; De La Haye et al., 2008; Lavvas et al., 2011), we suggested that the influx of charged particles in the auroral

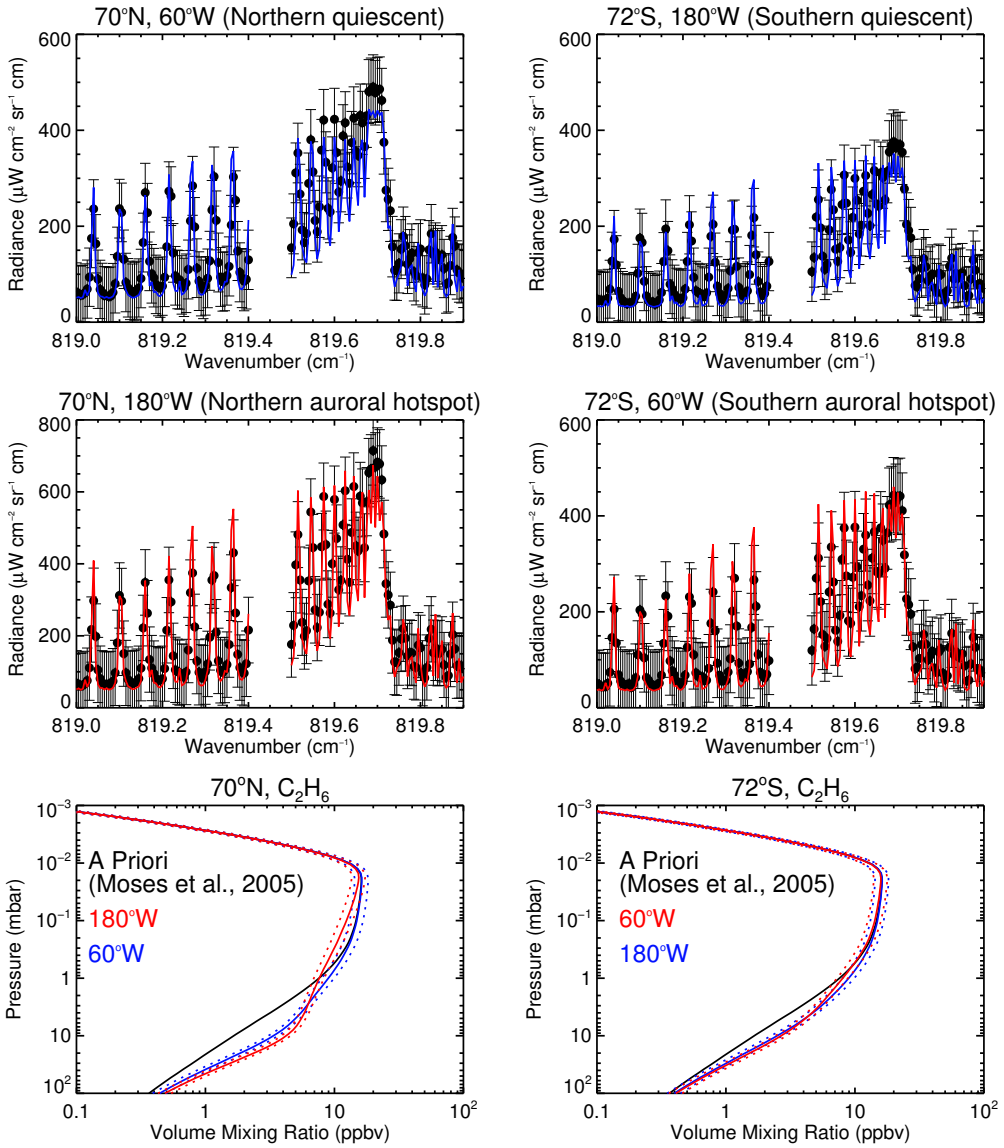

Figure 18: Model-data spectral comparisons at quiescent locations in the north (top, left) and south (top, right), the northern auroral hot spot (middle, left) and southern auroral hotspot (middle, right). Observed spectra are shown as points with error bars while modelled spectra are shown as coloured, solid lines. The corresponding retrieved vertical profiles of C_2H_6 are shown in the same colours in the bottom plots. As shown, there is negligible difference (within uncertainty) in C_2H_6 between the auroral regions and quiescent longitudes in the same latitude band.

stratosphere greatly increases the importance of ion-neutral chemistry reactions. These reactions increase the abundance of all the major hydrocarbons, but unsaturated species such as C_2H_2 and C_2H_4 in particular. However, horizontal advection transports these species outside the auroral region where neutral photochemistry dominates and by sequential hydrogen-atom addition, C_2H_2 and C_2H_4 are readily converted into C_2H_6 at deeper pressures. Thus, the chemistry is expected to yield an enrichment of C_2H_2 and C_2H_4 in auroral regions, with respect to quiescent longitudes, which our results show.

While concentrations of C_2H_6 retrieved from TEXES at the 1-mbar at high-northern latitudes do decrease in the auroral region, this change is not significant with respect to uncertainty as detailed above. Either longitudinal variations of C_2H_6 are too small to be measured at the sensitivity TEXES can provide or C_2H_6 is in fact longitudinally well-mixed at high-northern latitudes, at least in December 2014. C_2H_6 is chemically stable for longer than a Jupiter year (~12 years) at the 1-mbar level and so once produced can be transported longitudinally by advection and diffusion on timescales shorter than its chemical lifetime. This might be expected to yield a longitudinally-well mixed distribution. In Sinclair et al. (2017a), using CIRS measurements acquired in 2001, we found that C_2H_6 was depleted (by greater than the 1-σ level) in the northern auroral region, with respect to quiescent longitudes. We suggested this was a result of C_2H_6 being produced from C_2H_2 and C_2H_4

(as detailed above) at quiescent longitudes thereby giving the impression its concentration was lower in the auroral region. Perhaps this result was an artefact of CIRS' lower spectral resolution and therefore vertical sensitivity in the atmosphere and/or a transient feature in the longitudinal distribution of C_2H_6, perhaps due to a recent surge in production and conversion of C_2H_2 and C_2H_4. Again, our understanding of how the neutral hydrocarbons in the stratosphere are affected by the chemistry present in the auroral regions will be further tested and confirmed by determining their evolution in future measurements.

7. Conclusions

Retrievals of the vertical temperature profile and the vertical profiles of C_2H_2, C_2H_4 and C_2H_6 were performed using IRTF-TEXES (Texas Echelon Cross Echelle Spectrograph (Lacy et al., 2002) on NASA's Infrared Telescope Facility) observations acquired of Jupiter's high latitudes on December 10th-11th, 2014. In comparing results at 70°N, 180°W (the northern auroral region) and 70°N, 60°W (a representative 'quiescent' region), we found temperatures in the former to be elevated in two discrete pressure regions at approximately 1 mbar and 10 μbar. For example, temperatures from 70°N, 60°W to 70°N, 180°W increase by 19.0 ± 4.2 K at 0.98 mbar and 20.8 ± 3.9 K at 0.01 mbar but increase only by 8.3 ± 4.9 K at the intermediate level of 0.1 mbar. The temperature profile retrieved in the southern auroral region is also qualitatively similar. As in Sinclair et al. (2017a), we conclude that elevated temperatures at the 0.01-mbar level result from heating associated with ion and electron precipitation. We instead attribute the 1-mbar heating either to the precipitation of a higher-energy source of charged particles and/or haze particles produced by the auroral chemistry, which are heated by shortwave solar radiation.

C_2H_2 and C_2H_4 exhibit an enrichment in the northern auroral region with respect to quiescent longitudes in the same latitude band. However, C_2H_6 exhibits negligible change as a function of longitude at 70°N with respect to the uncertainty on retrieved concentrations. As discussed in Sinclair et al. (2017a) and by analogy with ion-neutral chemistry models developed for the atmosphere of Titan (De La Haye et al., 2008), we believe the influx of charged particles in Jupiter's auroral regions significantly increases the production of C_2H_2 and C_2H_4 through ion-neutral chemistry. These hydrocarbons are continuously produced in the auroral region but once advected longitudinally are readily converted into C_2H_6 by neutral chemistry (sequential H-atom addition). This yields an enrichment in the concentration of C_2H_2 and C_2H_4 in the northern auroral region with respect to quiescent longitudes, which our results show. Once produced, C_2H_6 is chemically stable for timescales longer than a Jupiter year (e.g. Moses et al. 2005, Figure 12 of Nixon et al. 2010) and so would be expected to become longitudinally well-mixed, which our results also indicate. The magnitude of uncertainties on retrieved hydrocarbon concentrations in the southern auroral region prevented us from making any assessment of how their concentrations are modified by the southern auroral region. Our above interpretations for the vertical temperature profile retrieved in the northern and southern auroral regions and the longitudinal variations in C_2H_2, C_2H_4 and C_2H_6 will be tested in future measurements.

8. Acknowledgements

Many thanks are due to the Infrared Telescope Facility, which is operated by the University of Hawaii under contract NNH14CK55B with the National Aeronautics and Space Administration. Many thanks to the NASA Postdoctoral Program (managed by Oak Ridge Associated Universities until February 2016 and subsequently by Universities Space Research Administration) for funding Sinclair during the analysis of this research. Orton was supported by grants from NASA to the Jet Propulsion Laboratory/California Institute of Techonology. Fletcher was supported by a Royal Society Fellowship at the University of Leicester and the remaining UK authors thanks the Science and Technologies Facilities Council (STFC) for their support.

9. References

B. Bonfond, D. Grodent, J.-C. Gérard, T. Stallard, J. T. Clarke, M. Yoneda, A. Radioti, and J. Gustin. Auroral evidence of Io's control over the magnetosphere of Jupiter. *Geophysical Research Letters*, 39:L01105, January 2012. doi: 10.1029/2011GL050253.

J. Caldwell, F. C. Gillett, and A. T. Tokunaga. Possible infrared aurorae on Jupiter. *Icarus*, 44:667–675, December 1980. doi: 10.1016/0019-1035(80)90135-9.

J. Caldwell, R. Halthore, G. Orton, and J. Bergstralh. Infrared polar brightenings on Jupiter. IV - Spatial properties of methane emission. *Icarus*, 74:331–339, May 1988. doi: 10.1016/0019-1035(88)90045-0.

B. J. Conrath, P. J. Gierasch, and S. S. Leroy. Temperature and circulation in the stratosphere of the outer planets. *Icarus*, 83:255–281, February 1990. doi: 10.1016/0019-1035(90)90068-K.

V. De La Haye, J. H. Waite, T. E. Cravens, I. P. Robertson, and S. Lebonnois. Coupled ion and neutral rotating model of Titan's upper atmosphere. *Icarus*, 197:110–136, September 2008. doi: 10.1016/j.icarus.2008.03.022.

P. Drossart, B. Bezard, S. K. Atreya, J. Bishop, J. H. Waite, Jr., and D. Boice. Thermal profiles in the auroral regions of Jupiter. *Journal of Geophysical Research*, 98:18803, October 1993. doi: 10.1029/93JE01801.

F M Flasar, V G Kunde, M M Abbas, R K Achterberg, P Ade, A Barucci, B Bézard, G L Bjoraker, J C Brasunas, and S Calcutt. Exploring the saturn system in the thermal infrared: The composite infrared spectrometer. *Space Science Reviews*, 115(1-4):169–297, 2004.

L. N. Fletcher, G. S. Orton, N. A. Teanby, and P. G. J. Irwin. Phosphine on Jupiter and Saturn from Cassini/CIRS. *Icarus*, 202:543–564, August 2009. doi: 10.1016/j.icarus.2009.03.023.

L. N. Fletcher, T. K. Greathouse, G. S. Orton, J. A. Sinclair, R. S. Giles, P. G. J. Irwin, and T. Encrenaz. Mid-infrared mapping of Jupiter's temperatures, aerosol opacity and chemical distributions with IRTF/TEXES. *Icarus*, 278:128–161, November 2016. doi: 10.1016/j.icarus.2016.06.008.

T. Fouchet, T. K. Greathouse, A. Spiga, L. N. Fletcher, S. Guerlet, J. Leconte, and G. S. Orton. Stratospheric aftermath of the 2010 Storm on Saturn as observed by the TEXES instrument. I. Temperature structure. *Icarus*, 277:196–214, October 2016. doi: 10.1016/j.icarus.2016.04.030.

A. J. Friedson, A.-S. Wong, and Y. L. Yung. Models for Polar Haze Formation in Jupiter's Stratosphere. *Icarus*, 158:389–400, August 2002. doi: 10.1006/icar.2002.6885.

R. Hanel, D. Crosby, L. Herath, D. Vanous, D. Collins, H. Creswick, C. Harris, and M. Rhodes. Infrared spectrometer for voyager. *Applied Optics*, 19: 1391–1400, May 1980. doi: 10.1364/AO.19.001391.

P. G. J. Irwin, N. A. Teanby, R. de Kok, L. N. Fletcher, C. J. A. Howett, C. C. C. Tsang, C. F. Wilson, S. B. Calcutt, C. A. Nixon, and P. D. Parrish. The NEMESIS planetary atmosphere radiative transfer and retrieval tool. *Journal of Quantitative Spectroscopy and Radiative Transfer*, 109: 1136–1150, April 2008.

S. J. Kim, J. Caldwell, A. R. Rivolo, R. Wagener, and G. S. Orton. Infrared polar brightening on Jupiter. III - Spectrometry from the Voyager 1 IRIS experiment. *Icarus*, 64:233–248, November 1985. doi: 10.1016/0019-1035(85)90088-0.

T. Kostiuk, P. Romani, F. Espenak, and T. A. Livengood. Temperature and abundances in the Jovian auroral stratosphere. 2: Ethylene as a probe of the microbar region. *Journal of Geophysical Research*, 98:18823, October 1993. doi: 10.1029/93JE01332.

T. Kostiuk, T. A. Livengood, Hewagama T., K. E. Fast, G. L. Bjoraker, F. Schmuelling, S. Guido, and J. R. Kolasinski. P33C-2155: Variability of Mid-Infrared Aurora on Jupiter: 1979 to 2016. In *American Geophysical Union Fall Meeting 2016. P33C: Juno's Exploration of Jupiter and the Earth-Based Collaborative Campaign III Posters*, 2016.

J. H. Lacy, M. J. Richter, T. K. Greathouse, D. T. Jaffe, and Q. Zhu. Texes: A sensitive high-resolution grating spectrograph for the mid-infrared. *Publications of the Astronomical Society of the Pacific*, 114:153–168, February 2002. doi: 10.1086/338730.

P. Lavvas, M. Galand, R. V. Yelle, A. N. Heays, B. R. Lewis, G. R. Lewis, and A. J. Coates. Energy deposition and primary chemical products in Titan's upper atmosphere. *Icarus*, 213:233–251, May 2011. doi: 10.1016/j.icarus.2011.03.001.

T. A. Livengood, T. Kostiuk, and F. Espenak. Temperature and abundances in the Jovian auroral stratosphere. 1: Ethane as a probe of the millibar region. *Journal of Geophysical Research*, 98:18813, October 1993. doi: 10.1029/93JE01043.

M. López-Puertas and F.W. Taylor. *Non-LTE Radiative Transfer in the Atmosphere*. Series on atmospheric, oceanic and planetary physics. World Scientific, 2001. ISBN 9789812811493. URL `https://books.google.com/books?id=1dC9l0q67SYC`.

J. I. Moses and T. K. Greathouse. Latitudinal and seasonal models of stratospheric photochemistry on Saturn: Comparison with infrared data from IRTF/TEXES. *Journal of Geophysical Research (Planets)*, 110: E09007, September 2005. doi: 10.1029/2005JE002450.

J. I. Moses, T. Fouchet, B. Bézard, G. R. Gladstone, E. Lellouch, and H. Feuchtgruber. Photochemistry and diffusion in Jupiter's stratosphere: Constraints from ISO observations and comparisons with other giant planets. *Journal of Geophysical Research (Planets)*, 110:E08001, August 2005. doi: 10.1029/2005JE002411.

J. D. Nichols, E. J. Bunce, J. T. Clarke, S. W. H. Cowley, J.-C. Gérard, D. Grodent, and W. R. Pryor. Response of Jupiter's UV auroras to interplanetary conditions as observed by the Hubble Space Telescope during the Cassini flyby campaign. *Journal of Geophysical Research (Space Physics)*, 112:A02203, February 2007. doi: 10.1029/2006JA012005.

C. A. Nixon, R. K. Achterberg, B. J. Conrath, P. G. J. Irwin, N. A. Teanby, T. Fouchet, P. D. Parrish, P. N. Romani, M. Abbas, A. LeClair, D. Strobel, A. A. Simon-Miller, D. J. Jennings, F. M. Flasar, and V. G. Kunde. Meridional variations of C_2H_2 and C_2H_6 in Jupiter's atmosphere from Cassini CIRS infrared spectra. *Icarus*, 188:47–71, May 2007. doi: 10.1016/j.icarus.2006.11.016.

C. A. Nixon, R. K. Achterberg, P. N. Romani, M. Allen, X. Zhang, N. A. Teanby, P. G. J. Irwin, and F. M. Flasar. Abundances of Jupiter's trace hydrocarbons from Voyager and Cassini. *Planetary & Space Science*, 58: 1667–1680, November 2010. doi: 10.1016/j.pss.2010.05.008.

N. Ozak, D. R. Schultz, T. E. Cravens, V. Kharchenko, and Y.-W. Hui. Auroral X-ray emission at Jupiter: Depth effects. *Journal of Geophysical Research (Space Physics)*, 115(A14):A11306, November 2010. doi: 10.1029/2010JA015635.

P. N. Romani. Recent Rate Constant and Product Measurements of the Reactions C_2H_3 + $H_2$and C_2H_3 + H - Importance for Photochemical Modeling of Hydrocarbons on Jupiter. *Icarus*, 122:233–241, August 1996. doi: 10.1006/icar.1996.0122.

A. A. Simon-Miller, B. J. Conrath, P. J. Gierasch, G. S. Orton, R. K. Achterberg, F. M. Flasar, and B. M. Fisher. Jupiter's atmospheric temperatures: From Voyager IRIS to Cassini CIRS. *Icarus*, 180:98–112, jan 2006. doi: 10.1016/j.icarus.2005.07.019.

J. A. Sinclair, G. S. Orton, T. K. Greathouse, Moses Fletcher, L. N., J. I., V. Hue, and P. G. J Irwin. Jupiter's auroral-related stratospheric heating and chemistry I: analysis of Voyager-IRIS and Cassini-CIRS spectra. *Icarus*, 292:182–207, December 2017a. doi: http://dx.doi.org/10.1016/j.icarus.2016.12.033.

T. S. Stallard, A. Masters, S. Miller, H. Melin, E. J. Bunce, C. S. Arridge, N. Achilleos, M. K. Dougherty, and S. W. H. Cowley. Saturn's auroral/polar H_3^+ infrared emission: The effect of solar wind compression. *Journal of Geophysical Research (Space Physics)*, 117(A16):A12302, December 2012. doi: 10.1029/2012JA018201.

V. Vuitton, R. V. Yelle, and M. J. McEwan. Ion chemistry and N-containing molecules in Titan's upper atmosphere. *Icarus*, 191:722–742, November 2007. doi: 10.1016/j.icarus.2007.06.023.

V. Vuitton, R. V. Yelle, and J. Cui. Formation and distribution of benzene on Titan. *Journal of Geophysical Research (Planets)*, 113:E05007, May 2008. doi: 10.1029/2007JE002997.

A.-S. Wong, A. Y. T. Lee, Y. L. Yung, and J. M. Ajello. Jupiter: Aerosol Chemistry in the Polar Atmosphere. *Astrophysical Journal Letters*, 534: L215–L217, May 2000. doi: 10.1086/312675.

A.-S. Wong, Y. L. Yung, and A. J. Friedson. Benzene and Haze Formation in the Polar Atmosphere of Jupiter. *Geophysical Research Letters*, 30:1447, April 2003. doi: 10.1029/2002GL016661.

X. Zhang, R. A. West, P. G. J. Irwin, C. A. Nixon, and Y. L. Yung. Aerosol influence on energy balance of the middle atmosphere of Jupiter. *Nature Communications*, 6:10231, December 2015. doi: 10.1038/ncomms10231.

Appendix A. Radiometric calibration adjustments

Appendix A.1. 587 cm^{-1}, 1248 cm^{-1}

The vertical temperature profile was retrieved simultaneously from the H_2 S(1) and CH_4 settings. In conducting preliminary retrievals, we discovered it was a challenge to simultaneously fit the observed H_2 S(1) emission and CH_4 emission with the same vertical temperature profile. While CH_4 emission features were generally fitted well by the modelled spectra, modelled radiances were generally higher than the observed radiances in the 587 cm^{-1} setting. It was concluded that the inability to fit these settings simultaneously was a result of some systematic radiometric offset in the 587 and/or 1248 setting.

In order to explore potential offsets in the radiometric calibration, we performed test temperature retrievals on spectra where the radiances in the 587 cm^{-1} and/or 1248 cm^{-1} settings were adjusted by a constant scale factor. At 70°N, 60°W, the spectra in the 587 cm^{-1} and 1248 settings were adjusted in radiance by scale factors ranging from 0.6 to 2.2 in steps of 0.025. This yielded a 2D grid of observed spectra spanning adjusted radiances in the 587 cm^{-1} and 1248 settings about the nominal calibration (a scale factor of 1). A similar 2D grid was then computed for the observations in both settings at 1) 70°N, 180°W, 2) 72°S, 60°W and 3) 72°S, 180°W in order to explore radiometric calibration at four different locations. For each location, the vertical temperature profile was retrieved across the 2D grid of observed spectra in each of these four locations, starting from the nominal temperature-pressure profile as the *a priori*.

Figure A.19 shows the reduced goodness-of-fit values for all these retrievals. The quality of the fit to the CH_4 spectra in the 1248 setting exhibits little variation as a function of the scale factor applied to the 587 cm^{-1} setting. This is true in all four locations covering quiescent and auroral longitudes at both high-southern and high-northern latitudes and is intuitive given that the number of spectra points in the 1248 cm^{-1} setting (approximately 580) greatly exceeds the 12 spectral points in the 587 cm^{-1} setting. The 1248 cm^{-1} setting is weighted relatively higher as the retrieval searches for the vertical temperature profile that minimises the fit to the observations.

In contrast, the quality of the fit to the 587 cm^{-1} setting exhibits a large variation as a result of radiometric adjustments in both the 587 cm^{-1} and 1248 settings. At all four locations, it is apparent that if the observed radiances in the 587 cm^{-1} setting are increased, those in the 1248 setting must also be increased in order for the same quality of fit to the 587 cm^{-1} spectra to be achieved. As demonstrated, the best fit to the observations is not achieved using the nominal calibration (scale factors of 1 applied to both settings). Instead, the best fit to the H_2 S(1) feature assuming the nominal calibration of the 587 cm^{-1} (a scale factor of 1) is achieved when the radiances in the 1248 setting are reduced by 20 - 40%. Conversely, the best fit to the H_2 S(1) feature assuming the nominal calibration of the 1248 setting is achieved when the 587 cm^{-1} radiances are increased by 20 - 40%.

In general, there were many combinations of adjusted radiances in the 587 cm^{-1} and 1248 settings for which the goodness-of-fit to the spectra was optimised. Figure A.20 shows a subset of the results shown in Figure A.19, where the radiances in the 1248 setting were fixed at the nominal calibration. In order to demonstrate that the relatively poorer fit of the modelled spectra to the observed spectra using the nominal calibration was not an artefact of the chosen *a priori* temperature profile, we performed further retrievals using an alternative *a priori*, where temperatures were made isothermal at 160 K at pressures lower than 10 mbar. These results are also presented in Figure A.20. As shown, regardless of the chosen temperature *a priori*, a systematic increase in the radiances in the 587 cm^{-1} by approximately 25% is required to minimise the fit to the spectra.

For all subsequent analyses, we opted to increase radiances in the 587 cm^{-1} setting by 25% but keep radiances in the 1248 setting fixed at their nominal value (a scale factor of 1 with respect to the nominal calibration). Our justifications for increasing the 587 cm^{-1} and not decreasing the 1248 setting, or increasing both settings, are as follows. Firstly, the 587 cm^{-1} spectra were measured with larger slit dimensions and thus the spatial footprint on the planet in a single pixel was larger than in the 730, 819, 950 and 1248 settings, which used a smaller slit width/length. In addition, the diffraction-limited spatial resolution is poorer at 587 cm^{-1} (1.43“) than in the higher wavenumber settings (e.g. ∼1.02“ at 819 cm^{-1}). Thus, relatively larger beam dilution is expected in the 587 cm^{-1} setting with respect to higher wavenumber settings and so a required increase in radiance with respect to the nominal calibration was expected. Secondly, as demonstrated in Section 4.4, we find that retrieved temperatures from TEXES at the 1-mbar level are systematically cooler than those retrieved by CIRS in 2000 (Sinclair et al., 2017a). While readers may interpret this as justification to increase the 1248 radiances also, it was uncertain how much of this temperature difference is a result of systematic radiometric calibration offsets or physical evolution of the planet between 2000 and 2014. However, the systematic offset in CIRS and TEXES results in CH_4 emission at least indicates that a decrease in the 1248 setting of TEXES spectra would be counterintuitive since it would increase the disagreement between CIRS and TEXES.

Figure A.21 shows model-data comparisons and retrieved temperature profiles using the nominal and adjusted radiometric calibration, where radiances in the 587 cm^{-1} setting were increased by 25% . In adjusting the calibration of the 587 cm^{-1} setting, the largest change in retrieved temperature occurs in the 300- to 30-mbar level sounded by the continuum adjacent to the H_2 S(1) feature. However, at stratospheric altitudes (10 - 0.001 mbar), the retrieved temperatures exhibit little difference. Thus, our adustment of the radiometric calibration of the 587 cm^{-1} setting only improves the fit to the observations and does not remove/change the results in the stratosphere of which the study has focused.

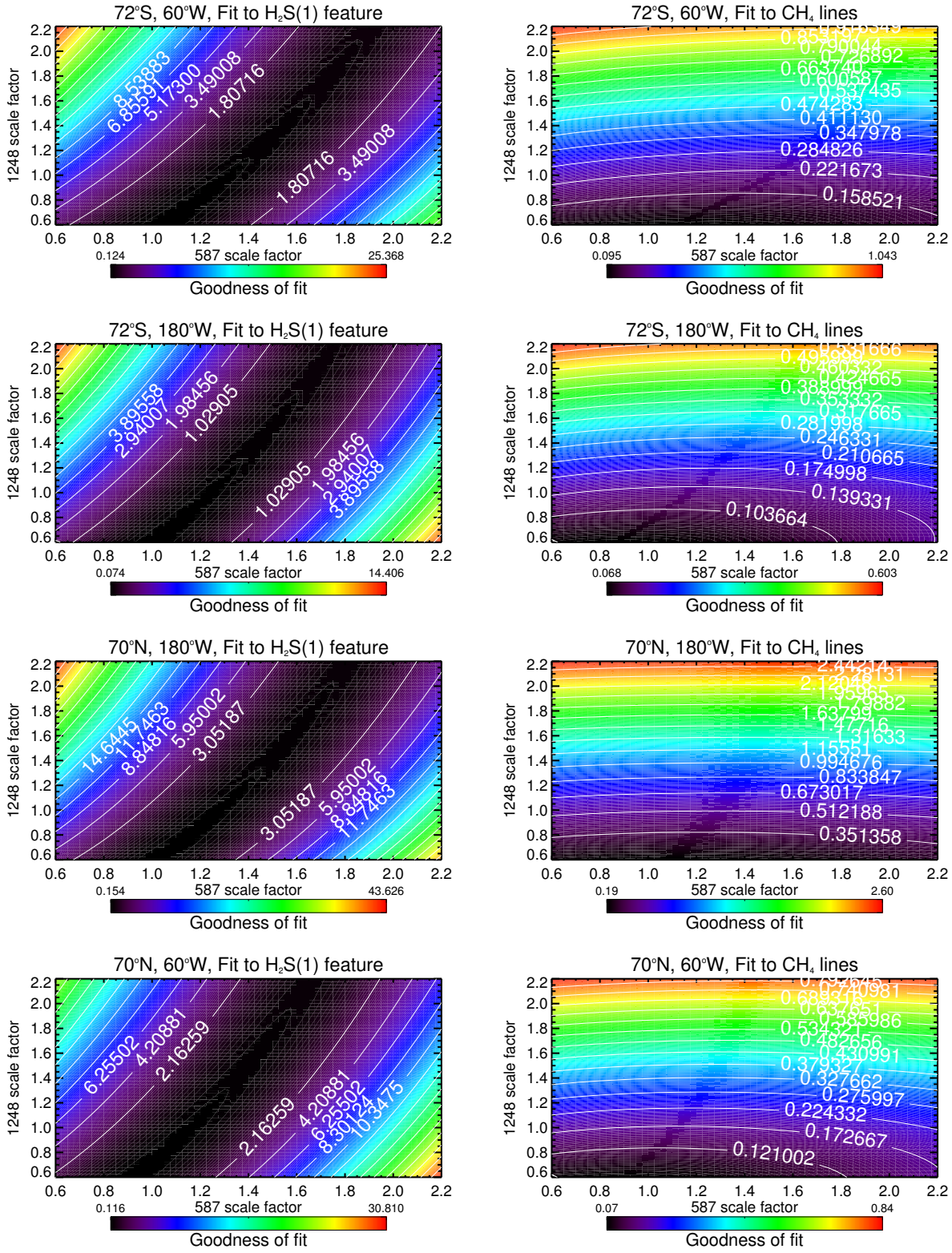

Figure A.19: The reduced goodness-of-fit values to the H_2 S(1) (left) and CH_4 emission spectra (right) with respect to scale factors applied to radiances in the 587 cm^{-1} and 1248 cm^{-1} settings at 72°S, 60°W (top), 72°S, 180°W (2nd row), 70°N 180°W (3rd row) and 70°N, 180°W (bottom).

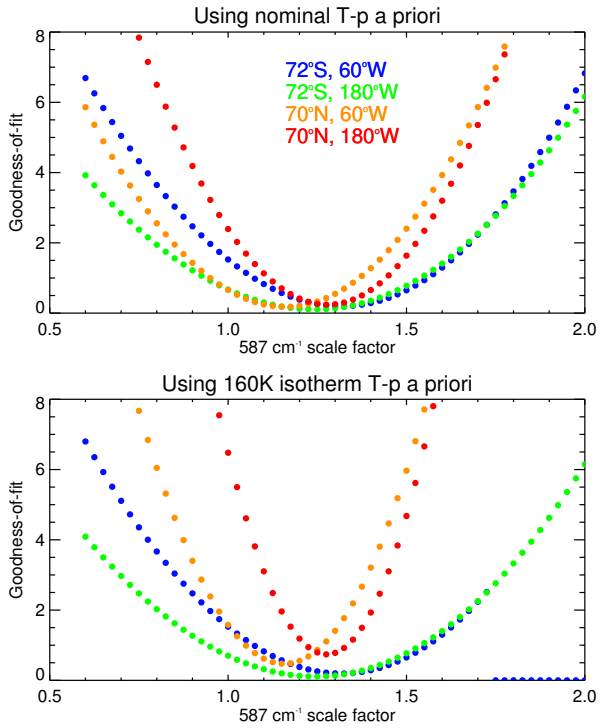

Figure A.20: The goodness-of-fit to the 587 cm^{-1} setting at 72°S, 60°W (blue), 72°S, 180°W (green), 70°N, 60°W (orange), 70°N, 180°W (red) as a function of the scale factor applied to the radiances in the 587 cm^{-1} setting. 1248 radiances were fixed at the nominal calibration. The top plot shows the results usng the nominal temperature-pressure profile as the *a priori*, the bottom plots shows the results assuming an 160 K isotherm *a priori* in order to demonstrate that the results are similar regardless of which *a priori* was adopted.

Appendix A.2. 730 cm^{-1}, 819 cm^{-1}, 950 cm^{-1}

We also explored the radiometric calibration of the 730 cm^{-1}, 819 cm^{-1} and 950 cm^{-1} settings. A similar approach to the calibration tests performed of the 587 cm^{-1} and 1248 settings in the previous Section was adopted for these settings. Observed spectra were scaled in radiance by constants varying from 0.6 to 2.2, in steps of 0.025, and retrievals of C_2H_2, C_2H_4 and C_2H_6 were performed. This was also tested at four locations: 1) 70°N, 180°W, 2) 70°N, 60°W, 3) 72°S, 60°W and 4) 72°S, 180°W to determine whether a systematic offset in radiance led to improved correspondence between modelled and observed spectra. However, we opted to use the nominal radiometric calibration (a scale factor of 1) in all of the 730 cm^{-1}, 819 cm^{-1} and 950 cm^{-1} settings. The reasoning for this decision is as follows.

In contrast to the results for the 587 cm^{-1} and 1248 settings detailed in the previous Section (Section Appendix A.1), there was no clear indication that a systematic increase or decrease in the radiances in the 730 cm^{-1}, 819 cm^{-1} and 950 cm^{-1} would improve the correspondence between modelled and observed spectra. Figure A.22 shows the variations in the goodness-of-fit parameter as a function of the scale factor applied to the radiances in the four locations tested.

819 cm^{-1}, 950 cm^{-1}: For the 819 cm^{-1} observations, while the fit to the spectra degraded when radiances were scaled by a factor of 1.4 or more, the quality of the fit exhibits negligible change when the radiances were varied by ±40% of the nominal calibration. This is true regardless of which C_2H_6 *a priori* profile was adopted. For the 950 cm^{-1} observations, there was greater variation in the quality of the fit to the observations as a function of the scale factor applied to the radiances. However, in all four locations and regardless of the different *a priori* profiles of C_2H_4 tested, the goodness-of-fit minimised when radiances were scaled in the range from 0.6 to 1.1.

730 cm^{-1}: The results for the 730 cm^{-1} observations were initially more challenging to interpret given the conflicting trends at the four locations tested. In both southern (auroral and quiescent) locations and at 70°N, 60°W, the trends of the goodness-of-fit suggest that radiances 20% - 80% higher than the nominal calibration are required to obtain the best fit to the spectra. However, testing of the retrievals at these locations with different *a priori* improved the fit to the spectra using the

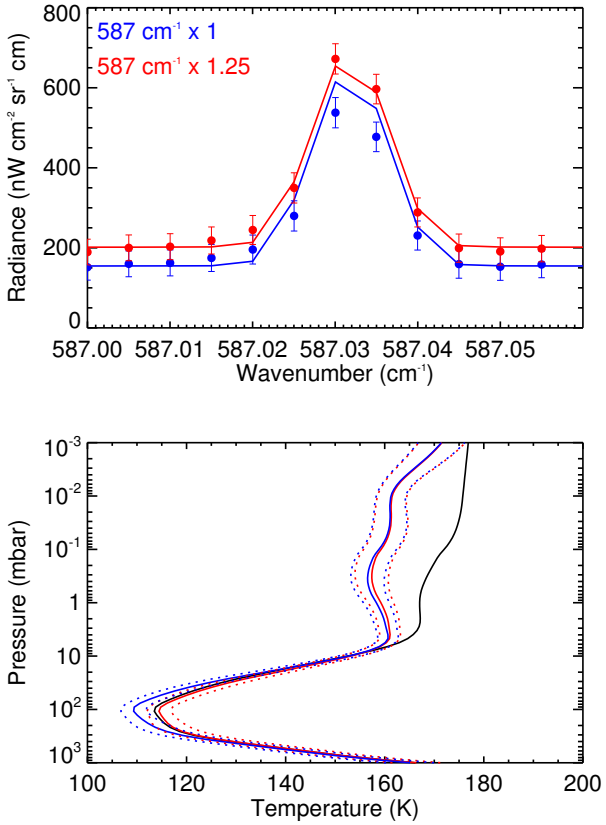

Figure A.21: A comparison of retrieved temperature profiles at 70°N, 60°W using the nominal (blue) and adjusted radiometric calibration (red) in the 587 cm^{-1} setting. As shown, the systematic 25% increase in radiances in the 587 cm^{-1} setting improves the fit between observed and modelled spectra without imposing qualitative differences in the retrieved vertical profile.

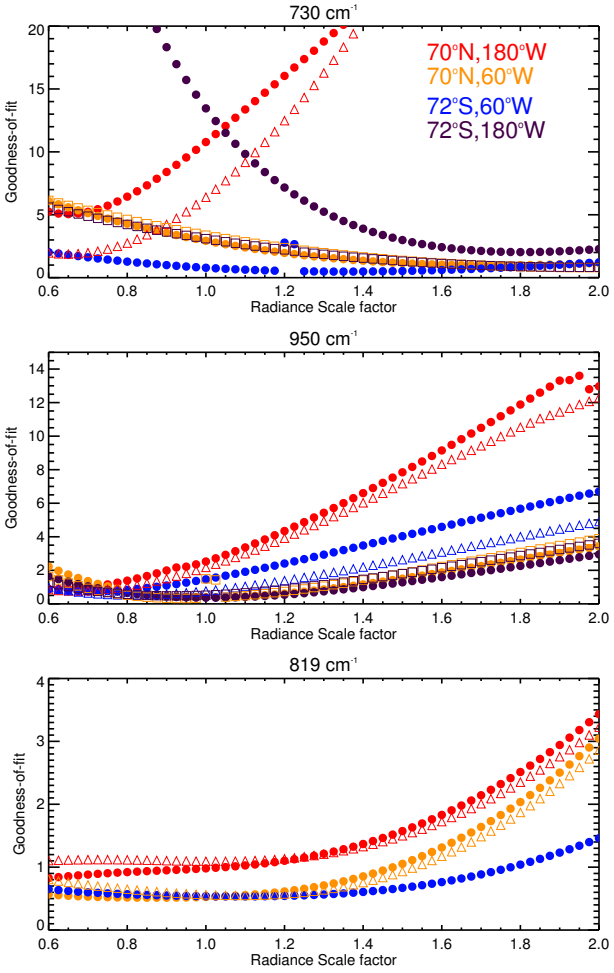

Figure A.22: Variations in the reduced goodness-of-fit between observed and modelled spectra as a function of the scale factor applied to radiances in the 730 cm^{-1} (top), 950 cm^{-1} (middle) and 819 cm^{-1} (bottom). Red results correspond to 70°N, 180°W, orange results correspond to 70°N, 60°W, blue results to 72°S, 60°W and purple results to 72°S, 180°W. Filled circles correspond to retrievals using the nominal reference profile of the appropriate hydrocarbon as *a priori*, unfilled triangles use the nominal profile multiple by a factor of 2 at all altitudes as the *a priori*.

nominal calibration. At 70°N, 180°W, we believe the apparent need for a decrease in observed radiances results from the presence of non-LTE (non local thermodynamic equilibrium) emission in the cores of the strongest C_2H_2 lines, which probe the upper stratosphere (1 - 10 µbar, Figure 10), as discussed in Section 5.4. So, as for the 819 and 950 cm^{-1} settings, there is no obvious indication that a systematic adjustment in the radiances is required.

Figure A.23 shows the fit to the observations at 70°N, 60°W in all three spectral settings using the nominal radiometric calibration. As demonstrated, the modelled radiances match those observed within the 1-σ level. Thus, visually, there is also no evidence of a need for a systematic increase or decrease in radiances in either of the 730 cm^{-1}, 819 cm^{-1} and 950 cm^{-1} settings in contrast to the 587 cm^{-1} and 1248 observations in the previous Section (Section Appendix A.1). Thus, in the absence of any clear indication that a systematic shift in radiance was necessary to improve the fit to the observations, we opted to use the nominal radiometric calibration.

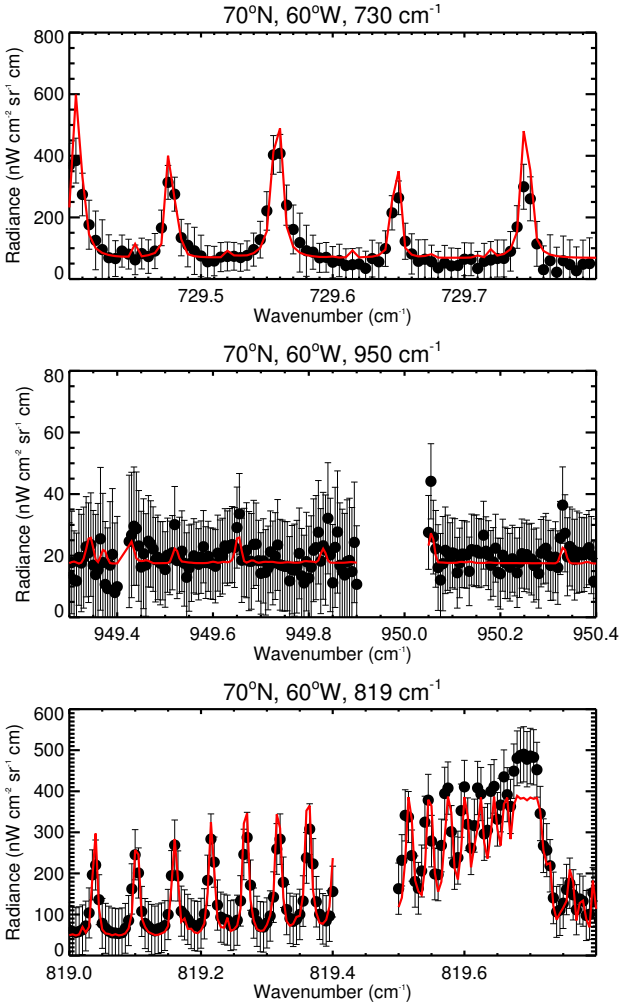

Figure A.23: A comparison of observed (black points with error bars) and modelled spectra (solid red) in the 730 cm^{-1} (top) , 950 cm^{-1} (middle) and 819 cm^{-1} (bottom) settings at 70°N, 60°W using the nominal radiometric calibration in all spectral settings.